NeuroImage 189 (2019) 55–70

Contents lists available at ScienceDirect

NeuroImage

journal homepage: www.elsevier.com/locate/neuroimage

Unbiased age-specific structural brain atlases for Chinese pediatric population

Tengda Zhao [a,b,c], Xuhong Liao [a,b,d], Vladimir S. Fonov [e], Qiushi Wang [a,b,c], Weiwei Men [f,g], Yanpei Wang [a], Shaozheng Qin [a,b,c], Shuping Tan [h], Jia-Hong Gao [f,g,i], Alan Evans [e,j,k], Sha Tao [a], Qi Dong [a], Yong He [a,b,c,*]

[a] National Key Laboratory of Cognitive Neuroscience and Learning, Beijing Normal University, Beijing, 100875, China
[b] Beijing Key Laboratory of Brain Imaging and Connectomics, Beijing Normal University, Beijing, 100875, China
[c] IDG/McGovern Institute for Brain Research, Beijing Normal University, Beijing, 100875, China
[d] School of Systems Science, Beijing Normal University, Beijing, 100875, China
[e] McConnell Brain Imaging Centre, Montreal Neurological Institute, McGill University, Montreal, Canada
[f] Center for MRI Research, Academy for Advanced Interdisciplinary Studies, Peking University, Beijing, 100871, China
[g] Beijing City Key Laboratory for Medical Physics and Engineering, Institute of Heavy Ion Physics, School of Physics, Peking University, Beijing, 100871, China
[h] Psychiatry Research Center, Beijing HuiLongGuan Hospital, Peking University, Beijing, 100096, China
[i] McGovern Institute for Brain Research, Peking University, Beijing, 100871, China
[j] McGill Centre for Integrative Neuroscience, Montreal Neurological Institute, McGill University, Montreal, Canada
[k] Ludmer Centre for NeuroInformatics and Mental Health, McGill University, Montreal, Canada

ARTICLE INFO

Keywords:
Brain template
Brain age
Machine learning
Development
MRI

ABSTRACT

In magnetic resonance (MR) imaging studies of child brain development, structural brain atlases usually serve as important references for the pediatric population, in which individual images are spatially normalized into a common or standard stereotactic space. However, the popular existing pediatric brain atlases (e.g., National Institutes of Health pediatric atlases, NIH-PD) are mostly based on MR images obtained from Caucasian populations and thus are not ideal for the characterization of the brains of Chinese children due to neuroanatomical differences related to genetic and environmental factors. Here, we use an unbiased template construction algorithm to create a set of age-specific Chinese pediatric (CHN-PD) atlases based on high-quality T1-and T2-weighted MR images from 328 cognitively normal Chinese children aged 6–12 years. The CHN-PD brain atlases include asymmetric and symmetric templates, sex-specific templates and tissue probability templates, and contain multiple age-specific templates at one-year intervals. A direct comparison of the CHN-PD and NIH-PD atlases reveals dramatic anatomical differences mainly in the bilateral frontal and parietal regions. After applying the CHN-PD and NIH-PD atlases to two independent Chinese pediatric datasets (N = 114 and N = 71), we find that the CHN-PD atlases result in significantly higher accuracy than the NIH-PD atlases in both predicting "brain age" and guiding brain tissue segmentation. These results suggest that the CHN-PD brain atlases are necessary for studies of the typical and atypical development of the Chinese pediatric population. These CHN-PD atlases have been released on the Neuroimaging Informatics Tools and Resources Clearinghouse (NITRC) website (https://www.nitrc.org/projects/chn-pd).

1. Introduction

Modern advances in multi-modal magnetic resonance imaging (MRI) offer an unprecedented opportunity to explore the structural and functional development of the pediatric brain *in vivo*. The typical research framework is achieved by normalizing individual brain images into a common or standard stereotactic space using a prior structural atlas, such as the International Consortium for Brain Mapping (ICBM152) templates (Evans et al., 2012; Lancaster et al., 2007), as a reference (Ashburner and Friston, 1999; Collins et al., 1998; Smith et al., 2004). Due to the rapid

* Corresponding author. National Key Laboratory of Cognitive Neuroscience and Learning, Beijing Key Laboratory of Brain Imaging and Connectomics, IDG/McGovern Institute for Brain Research, Beijing Normal University, Beijing, 100875, China.
E-mail address: yong.he@bnu.edu.cn (Y. He).

https://doi.org/10.1016/j.neuroimage.2019.01.006
Received 28 August 2018; Received in revised form 24 December 2018; Accepted 4 January 2019
Available online 6 January 2019
1053-8119/

development of the brain, structural atlases specific for young children have been generated for pediatric MRI investigations (Avants et al., 2015; Fonov et al., 2011; Luo et al., 2014; Oishi et al., 2019; Richards et al., 2016; Sanchez et al., 2012; Uchiyama et al., 2013; Wilke et al., 2002; Wu et al., 2016; Xie et al., 2015) (for a review, see (Dickie et al., 2017)). Compared with the employment of an adult atlas, adopting age-specific brain atlases for pediatric participants has been suggested to reduce the requirement for spatial deformation during image normalization and maintain a great number of pediatric characteristics of individual brains, such as a thicker cerebral cortex (Fonov et al., 2011; Yoon et al., 2009). However, the existing pediatric brain atlases are mostly based on Caucasian populations (Fonov et al., 2011; Richards et al., 2016; Sanchez et al., 2012; Wilke et al., 2002, 2008), and typically, the widely used National Institutes of Health pediatric (NIH-PD) atlases (Fonov et al., 2011). These existing brain atlases are not ideal for use in Chinese pediatric studies (Richards and Xie, 2015), since Chinese adults and children have unique neuroanatomical features that differ from those in Caucasian people in terms of brain morphology (Bai et al., 2012; Liang et al., 2015; Tang et al., 2010, 2018; Xie et al., 2015). Furthermore, different growth trajectories of brain structures have also been reported between Chinese and North American children (Guo et al., 2007; Xie et al., 2014). Therefore, creating age-specific atlases based on MR images of Chinese children is necessary to accurately represent the brains of Chinese pediatric populations.

During the construction of pediatric brain atlases, there are two important factors that need to be considered: brain asymmetry and sex differences. i) Brain asymmetry. The development of a child's brain is inherently asymmetric in both structure and function (Agcaoglu et al., 2015; Song et al., 2014; Zhong et al., 2016; Zhou et al., 2013). Asymmetric atlases which separately represent the left and right hemispheres, are naturally needed to provide an accurate representation of the children brain. Moreover, the degree of brain asymmetry is related to the specialization of language and motor functions and may underlie phenotypes of developmental disorders (Herbert et al., 2002; Shaw et al., 2009; Toga and Thompson, 2003). Symmetric atlases that treat both hemispheres equally are also needed for a quantitative description of the degree of brain asymmetry. Both asymmetric and symmetric brain atlases have been created for Caucasian pediatric populations (Fonov et al., 2011; Richards et al., 2016; Sanchez et al., 2012; Wilke et al., 2002, 2008). However, Chinese children have different brain asymmetries that differ from those in Caucasian children due to genetic and cultural factors. The visual processing of Chinese characters involves less lateralized brain function than the visual processing of alphabetic languages (Cao et al., 2009; Mei et al., 2015; Xue et al., 2005). The developmental disorders accompanied by asymmetric abnormalities, such as dyslexia (Beaton, 1997; Leonard and Eckert, 2008), are also marked by unique disruptions in the brains of Chinese children (Siok et al., 2004, 2008). Moreover, ethnic Chinese adults also exhibited significant morphological differences in several frontal and parietal regions compared with Caucasian adults (Chee et al., 2011; Tang et al., 2018). Therefore, the construction of both asymmetric and symmetric brain atlases is important for Chinese pediatric population. ii) Sex differences. Previous studies have reported sex-specific differences in the brain anatomy of typically and atypically developing populations (De Bellis et al., 2001; Evans et al., 2014; Gennatas et al., 2017; Good et al., 2001; Peper et al., 2011). Developmental disorders, such as attention-deficit/hyperactivity disorder (ADHD), are associated with sex-specific prevalence and symptomatology (Vértes and Bullmore, 2015). For an extreme example, sex chromosome-related disorders occur only in single-sex populations (Cutter et al., 2006; Murphy et al., 1993). In these situations, sex-specific atlases can be used to characterize the pediatric brain more accurately than atlases generated based on a mixed-sex population.

To date, only two structural MRI studies have been performed for the construction of Chinese pediatric brain atlases (Luo et al., 2014; Xie et al., 2015). Specifically, Luo et al. (2014) built a single brain template for pediatrics within a narrow age range of 5–8 years old using structural MR images of 53 Chinese children. Xie et al. (2015) generated a series of pediatric brain templates based on structural MR images of 138 Chinese children within an age range of 8–16 years at 2-year intervals. However, the applications of these two sets of brain atlases to Chinese pediatric studies is still limited due to several methodological issues (we will return to this issue in the Discussion section). Moreover, previous brain template studies only revealed the overall differences in the brain circumference and deformation costs during registration between the use of Chinese and Caucasian brain atlases (Liang et al., 2015; Tang et al., 2010; Xie et al., 2015). Considering the spatially distributed regional brain variations that potentially result from genetic and environmental effects during development, an examination of the detailed regional anatomical differences between Chinese and Caucasian pediatric brain atlases is important.

In the present study, we aimed to create a set of high-quality Chinese pediatric (CHN-PD) atlases depicting the brains of Chinese school-aged children from 6 to 12 years old. To achieve this goal, we first collected high-quality T1-and T2-weighted MR images of a large sample (328 participants) using a state-of-the-art 3T Siemens Prisma scanner. Then, we employed an unbiased template construction algorithm to generate a set of CHN-PD brain atlases, including average asymmetric and symmetric templates and sex-specific templates. Moreover, we also included the age-specific brain atlases at one-year intervals, which is a finer increment than that provided by previous studies. Finally, in a further exploration of the necessity and applicability of the proposed atlases, we compared regional anatomical differences between the CHN-PD and NIH-PD atlases, and further employed two independent Chinese pediatric datasets ($N = 114$ and $N = 71$) to evaluate the power of the CHN-PD and NIH-PD atlases in both predicting the "brain age" and guiding brain tissue segmentation.

2. Materials and methods

2.1. Participants

This study included the following three datasets comprising healthy Chinese children (Table 1): i) a principal dataset (Dataset 1) of 328 participants aged 6–12 years (9.03 ± 1.36) scanned at Peking University (PKU), ii) an independent dataset (Dataset 2) of 114 participants aged 6–12 years (9.06 ± 1.38) scanned at the Beijing HuiLongGuan (HLG) Hospital in China, and iii) another independent public dataset (Dataset 3) of 71 Chinese participants aged 8–12 years (10.26 ± 1.78) obtained from the Beijing site of the ADHD-200 dataset via the International Neuroimaging Data-sharing Initiative (Consortium, 2012; Fair et al., 2012). Datasets 1 and 2 were selected from the baseline dataset of a pediatric imaging genetic cohort study that recruited children from dozens of primary schools in Beijing. Written informed consents was obtained from the parents/guardians. Comprehensive assessments included multi-modal MRI scans of the brain, physical health, academic achievement, cognitive and non-cognitive functions for each child. A well-validated Chinese standardized cognitive ability test (Dong and Lin, 2011), including attention, visual-spatial, memory and reasoning abilities, was administered by a certified examiner and completed by each child within 90 min. The children whose data were included in this study were cognitively normal. The exclusion criteria included a history of neurological/psychiatric disorders, the use of psychoactive drugs, significant head injury and physical illness. The intake of any drugs or caffeine was prohibited on the day of the tests and MRI scans. In Dataset 3, the detailed information of the participants was accessed from the public data-sharing website of the ADHD-200 project (http://fcon_1000.projects.nitrc.org/indi/adhd200/). The initial collection of data included 359 participants in Dataset 1, 131 participants in Dataset 2 and 71 participants in Dataset 3. All MRI scans included here passed a strict quality control criteria. The detailed quality control procedure is described below. i) Individual images were subjected to a careful visual examination by an experienced radiologist (QW) to exclude incidental

Table 1
Demographic information of the three datasets.

	Age range (years)	Number	Sex (female/male)
Dataset 1 (PKU site)	6–12 (9.03 ± 1.36, 1.75)	328	153/175
Dataset 2 (HLG site)	6–12 (9.06 ± 1.38, 2.33)	114	47/67
Dataset 3 (Beijing site from ADHD-200)	8–12 (10.26 ± 1.78, 2.18)	71	46/25

PKU, Peking University; HLG, HuiLongGuan Hospital.
Age: MEAN ± STD, IQR.

abnormalities, including arachnoid cysts, neuroepithelial cysts and other intracranial space-occupying lesions. ii) Careful visual inspections with a scan rating procedure were separately conducted by two experienced raters (TZ and XL) using a protocol similar to that used in the Human Connectome Project (Marcus et al., 2013). iii) Images considered to have a better than fair quality by both raters were retained. This study was approved by the Ethics Committee of Beijing Normal University. Notably, Dataset 1 was used to construct the age-specific Chinese MRI atlases, and Datasets 2 and 3 were used to evaluate the atlas effects in both predicting the brain age and guiding brain tissue segmentation. Table 1 describes the age and sex distributions of the included samples.

2.2. Image acquisition

For Datasets 1 and 2, high-quality T1-and T2-weighted images were acquired for each participant using 3T Siemens Prisma scanners (separately at Peking University and HuiLongGuan Hospital). The detailed scanning parameters were as follows: 3D T1-weighted images: repetition time (TR) = 2530 ms, echo time (TE) = 2.98 ms, inversion time (TI) = 1100 ms, flip angle (FA) = 7°, acquisition matrix = 256 × 224, field of view (FOV) = 256 × 224 mm^2, number of slices = 192, in-plane resolution = 1.0 × 1.0 mm, slice thickness = 1.0 mm, bandwidth (BW) = 240 Hz/Px, scan time = 5 min and 58 s; T2-weighted images: 3D T2-SPACE sequence, TR = 3200 ms, TE = 564 ms, acquisition matrix = 320 × 320, FOV = 224 × 224 mm^2, slices = 256, in-plane resolution = 0.7 × 0.7 mm, slice thickness = 0.7 mm, BW = 744 Hz/Px, and scan time = 8 min and 24 s. In Dataset 3, the images were acquired using a 3T Siemens Trio scanner with the following scanning parameters: T1-weighted magnetization-prepared rapid acquisition gradient echo sequences, TR = 2530 ms, TE = 3.39 ms, TI = 1100 ms, FA = 7°, acquisition matrix = 256 × 256, FOV = 256 × 256 mm^2, 128 slices, slice thickness = 1.33 mm, and average = 1.

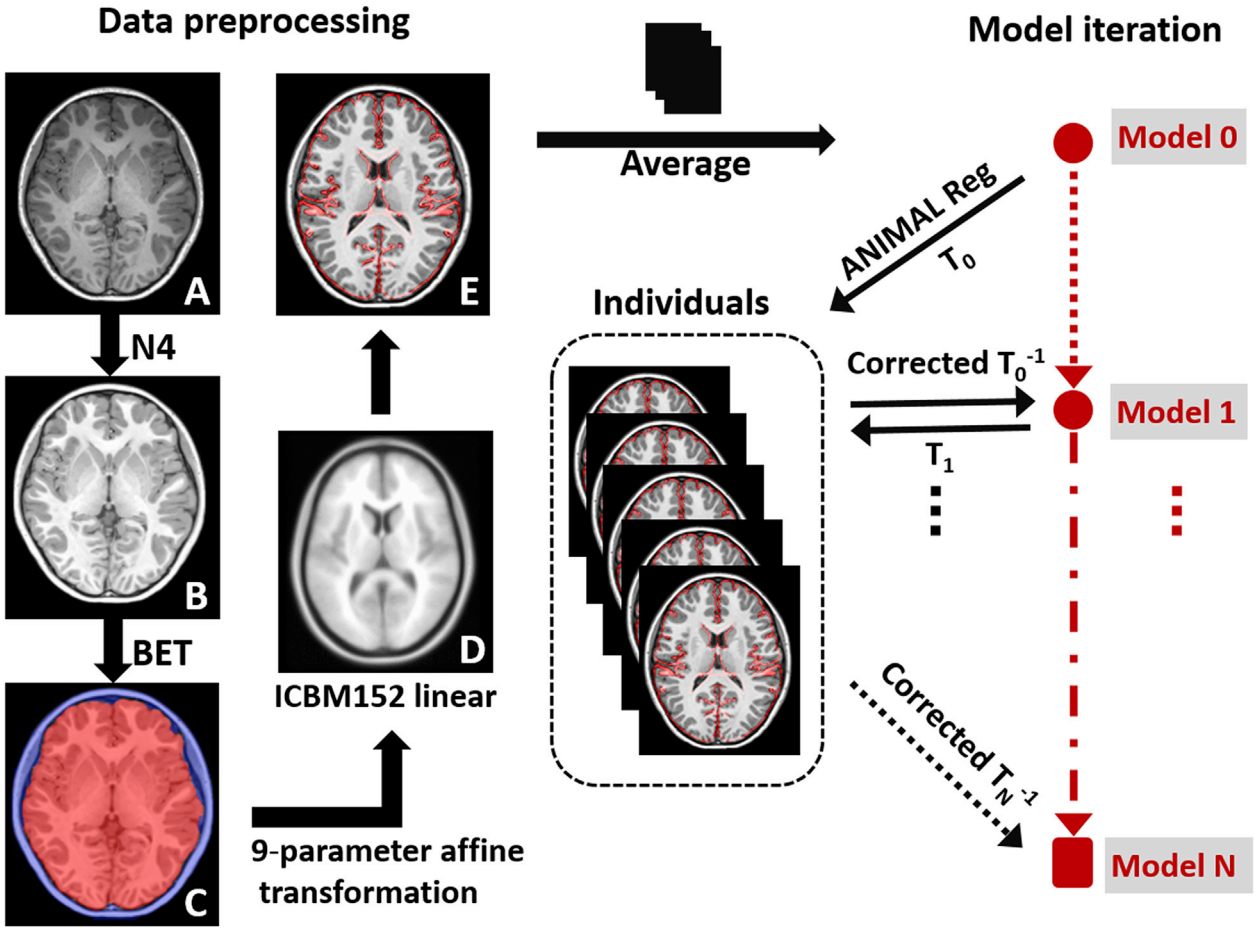

Fig. 1. Flowchart of the data preprocessing and template iteration process. Individual MRI scans (A) were first corrected for intensity inhomogeneity by using the N4 correction (B). The brain mask and skull outlines (C) were created using the robust BET estimation from the FSL. A hierarchical linear (nine-parameter affine transformation) registration of the individual image to the ICBM152 linear template (D) was conducted using the Revised BestLinReg algorithm, and the image intensity was scaled to the same range as the target (D). The resulting individual images (E) were averaged to generate the initial template (Model 0), which was used to further generate individual transformations (T_0) using the ANIMAL nonlinear registration. This deformation (T_0) was then corrected by the average transformation and applied to individual images (corrected T_0^{-1}) to create the new averaging approximation. This iterative process continued until convergence was reached.

Table 2
Demographic information of each age subgroup in Dataset 1 (PKU data).

	Age range (years)	Number	Sex (female/male)
Group 1	6–7	23	14/9
Group 2	7–8	53	25/28
Group 3	8–9	99	42/57
Group 4	9–10	87	42/45
Group 5	10–11	51	23/28
Group 6	11–12	34	16/18

2.3. Construction of pediatric brain atlases

All MRI scans were first preprocessed using the steps described below (Fig. 1, left panel). i) The intensity inhomogeneity of each scan was corrected using N4 correction (Tustison et al., 2010). ii) Brain masks were created using Brain Extraction Tool (BET) estimation and skull outlines were generated using BET2 (Smith, 2002). iii) A hierarchical linear registration (nine-parameter affine transformation) of each scan to the ICBM152 linear brain template was conducted using the Revised BestLinReg algorithm (Dadar et al., 2018). iv) The image intensity was scaled to the same range of the template (Nyúl and Udupa, 1999). v) Individual tissue segmentations were implemented using the well-validated CIVET 2.1 pipeline to obtain probability maps for the gray matter (GM), white matter (WM) and cerebrospinal fluid (CSF) (http://www.bic.mni.mcgill.ca/ServicesSoftware/CIVET-2-1-0-Table-of-Contents).

Next, the unbiased template construction algorithm was adopted to generate the pediatric brain atlas (Fig. 1, right panel). This procedure was proposed by Fonov and colleagues (Fonov et al., 2011) based on previous methods (Guimond et al., 1998, 2001), and has been widely applied to generate MRI templates, including the ICBM152 brain template, the NIH-PD brain template and the standard spinal cord template (De Leener et al., 2018; Fonov et al., 2009, 2011, 2014). Briefly, the preprocessed images were first averaged as the initial reference target template (Model 0) onto which each T1-weighted image was mapped nonlinearly. The generated individual transformations were further corrected using the averaging transformation to remove the bias. The new approximation was then generated by applying each corrected transformation to the corresponding individual T1-weighted image and then averaging all images together. The above process was iterated until convergence was reached. During each iteration, a nonlinear registration using Automatic Nonlinear Image Matching and Anatomical Labeling (ANIMAL) (Collins et al., 1995) was performed with an increasingly fine grid step size and blurring kernel. We adopted the following hierarchical schedule, which was the same schedule for the NIH-PD brain template (Fonov et al., 2011): 4 iterations at 32 mm, 4 iterations at 16 mm, 4 iterations at 8 mm, 4 iterations at 4 mm, and 4 iterations at 2 mm (the resolution of the deformation field). The T2-weighted brain atlases and the tissue probability atlases were created by warping the corresponding individual images using the final deformation field in the construction of the T1-weighted brain atlases and then by separately generating an average image.

We generated a set of Chinese pediatric atlases, including several different types based on the PKU dataset (Dataset 1). i) The asymmetric whole-head and brain-extracted MRI volumes were processed separately using the model iteration framework to generate both *head* and *brain* templates. ii) The symmetric brain templates were generated by including left-right flipped scans of each participant at the start and enforcing symmetric deformation fields in the whole iteration process. iii) The sex-specific brain templates were generated by using the MRI volumes of male and female participants separately. iv) We divided all participating children into six age subgroups with one-year intervals to generate the brain atlases specific for each age subrange (see Table 2 for detailed information about the participants in each age subgroup), and the whole template construction procedures were separately conducted for each group. Notably, the PKU data (Dataset 1) and our template construction procedure can also be used to generate customized pediatric templates according to different age ranges of interests (e.g., 7–9 years old).

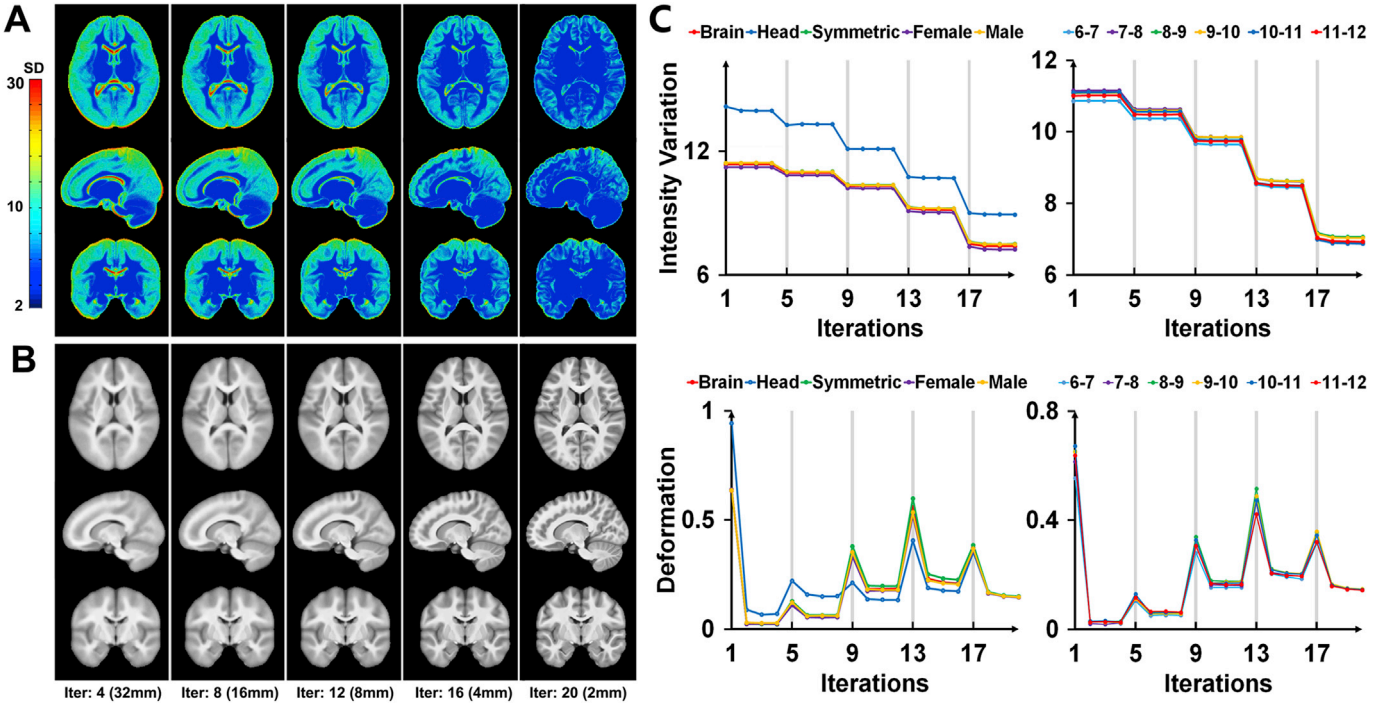

Fig. 2. The average MRI templates generated during the hierarchical matching process. (A) Color scale images show the intensity standard deviation of each averaged brain model at the specified step sizes during the iterative process. (B) Grayscale images show the average T1-weighted brain models at the corresponding steps. (C) The root mean square of the standard deviation of the intensity (upper panel) and the biases in the average deformation (lower panel) at each iteration are shown for the MRI templates of the full age range (left panel) and age subranges (right panel). The gray line shows the different blurring kernels used during the iterations.

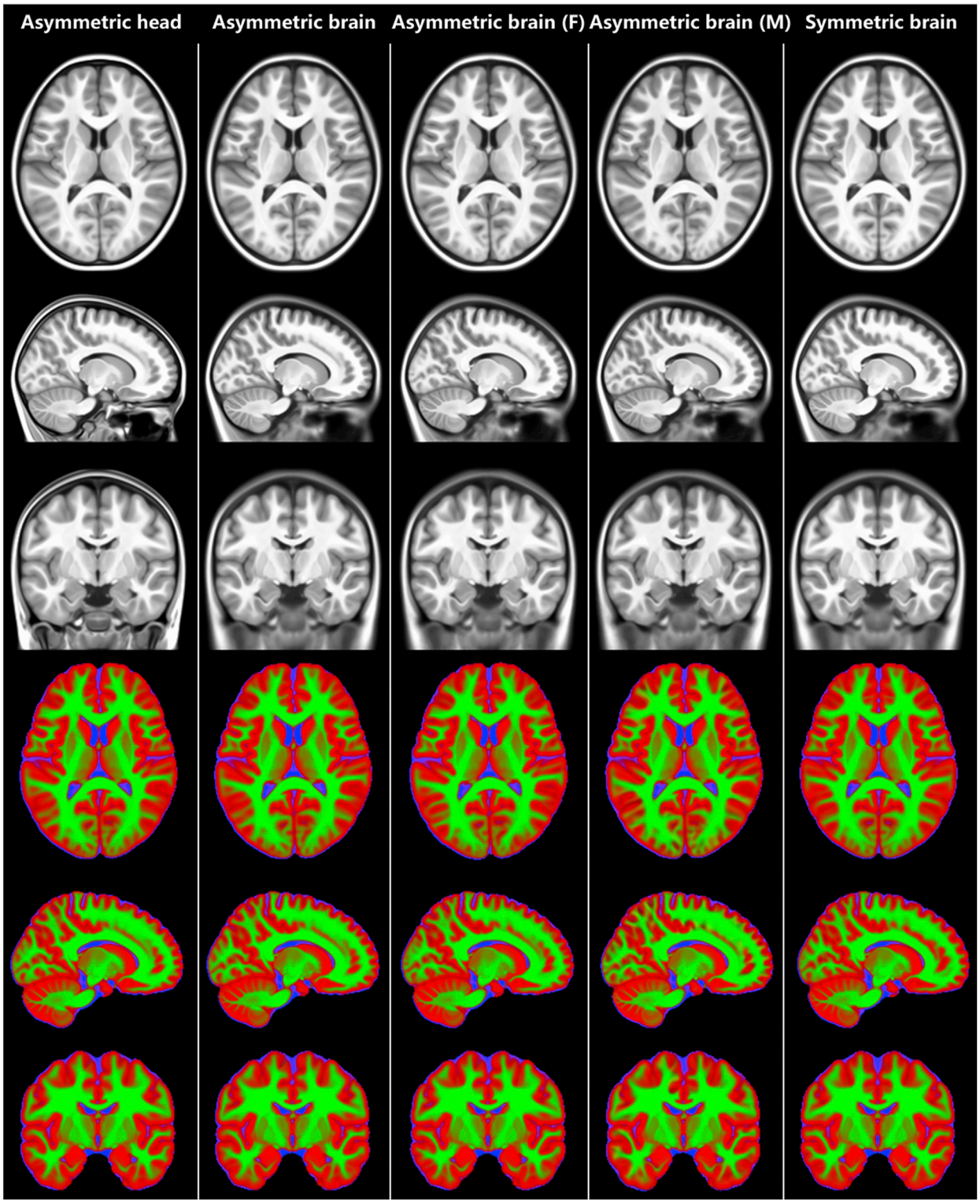

Fig. 3. Detailed slices of the Chinese pediatric atlases at a full age range (6–12 years old). The T1-weighted templates are shown in the upper panel and the tissue probability atlases are shown in the lower panel. These templates include the asymmetric head/brain templates, asymmetric sex-specific brain templates (F, female; M, male) and the symmetric brain template. GM, gray matter; WM, white matter; CSF, cerebrospinal fluid. The templates are displayed in the neurological convention.

2.4. Evaluation of regional anatomical differences between the brain atlases (CHN-PD vs. NIH-PD)

To estimate the regional anatomical differences between the proposed CHN-PD atlases and the commonly used NIH-PD atlases, we first extracted a subgroup of PKU children (Dataset 1) with the same age and sex distribution and used the same number of subjects as those in the group used to generate the NIH-PD template at 7- to 11-year-old. Using the data from this subgroup, a new Chinese pediatric brain template was created and used for the subsequent template evaluations to reduce the effect of sample distribution. Second, the NIH-PD brain template and tissue probability atlases were coregistered to this new Chinese template

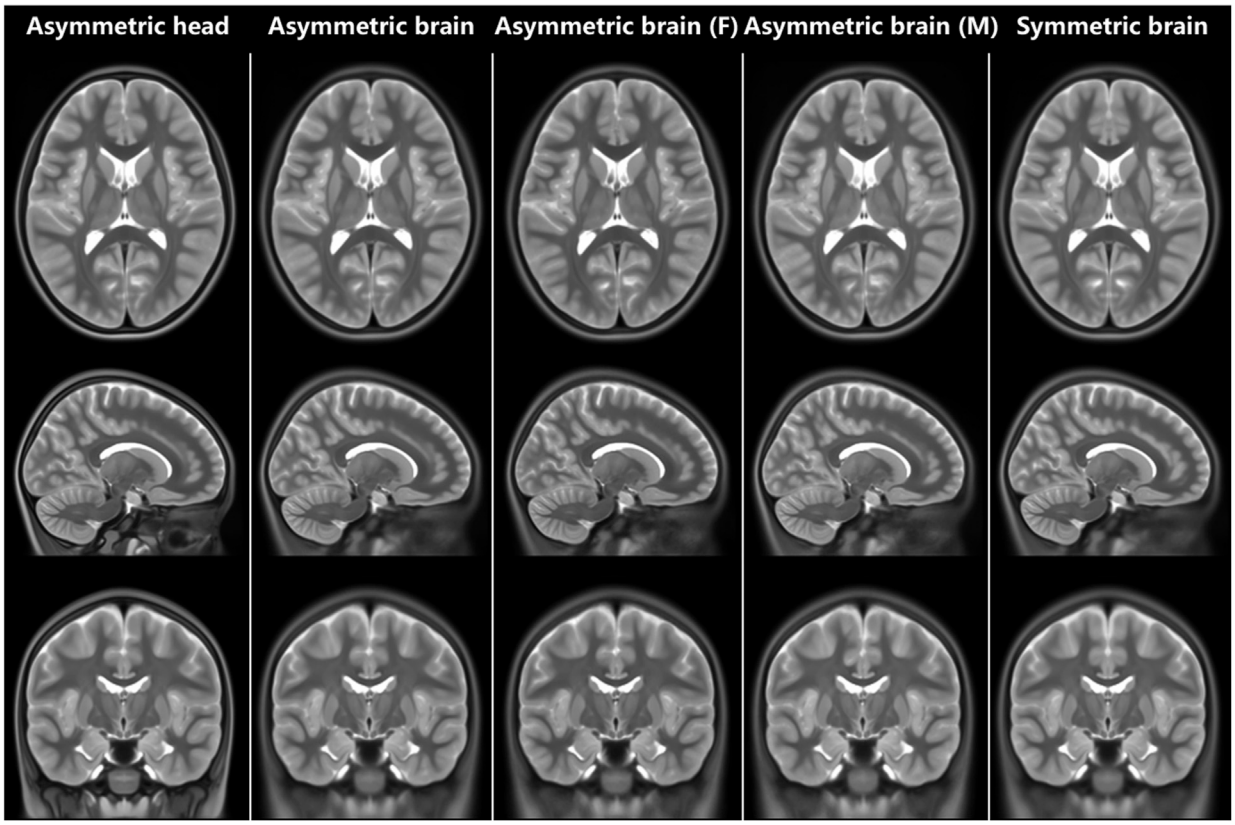

Fig. 4. Detailed slices of the T2-weighted Chinese pediatric atlases at a full age range (6–12 years old). These templates include the asymmetric head/brain templates, asymmetric sex-specific brain templates (F, female; M, male) and the symmetric brain template. The templates are displayed in the neurological convention.

with a linear nine-parameter affine transformation to reduce the effect of the brain circumference.

Instead of the usual visual inspections, we estimated the anatomical differences between the CHN-PD and NIH-PD brain atlases by calculating two quantitative image indexes in each Brodmann area. Specifically, the ICBM152 nonlinear template was first warped into the T1-weighted CHN-PD brain template using a nonlinear hierarchical ANIMAL registration (the T1-weighted NIH-PD template was used for a validation, see Supplemental Materials and Fig. S1). The generated transformation was applied to the Brodmann atlas to obtain the adjusted brain areas. Next, for each adjusted area, we calculated the mean square difference (MSD) (Holden et al., 2000) in the gray matter probability, which assesses the absolute differences in the gray matter morphology between the two brain atlases, and the normalized cross correlation (NCC) (Zhao et al., 2006), which reflects the spatial similarity of the anatomical structures between the two brain atlases. The details of these two indexes are described in the Supplemental Materials.

2.5. Evaluation of the atlases effects (CHN-PD vs. NIH-PD) on the accuracy of brain age prediction

To determine whether the proposed CHN-PD atlases have advantages over Caucasian pediatric brain atlases in studies regarding Chinese children, we performed a comparative analysis to evaluate their prediction power for brain age. Here, we employed the CHN-PD brain template that were generated using Dataset 1 subsamples with matched age and sex as those of the NIH-PD template at 7–11 years old (see above section). To reduce the overfitting effect, we used two independent datasets (Dataset 2 and Dataset 3) in training and testing the brain age prediction model in turns. The main process is described below. First, Dataset 2 was used as the training sample, and Dataset 3 was used as the testing sample. For each subject, the T1-weighted image was separately normalized to the new Chinese pediatric template and to the NIH-PD template using the hierarchical ANIMAL nonlinear registration. Second, the Brodmann mask was warped separately into the two brain templates using a nonlinear transformation that was obtained using the registration between the ICBM152 template and the CHN-PD/NIH-PD template to locate feature voxels for the prediction model. Next, we implemented the two most widely used machine-learning regression strategies (Cui and Gong, 2018; Drucker et al., 1997; Tipping, 2001) to predict individual age based on the normalized T1-weighted images. The first strategy was a support-vector regression (SVR) model with a linear kernel function (Drucker et al., 1997). Common settings, $C = 1$ and epsilon $= 0.001$, were adopted. The second strategy was the relevance vector regression (RVR), which is a Bayesian-formulated regression framework (Tipping, 2001). After model training and testing, the Pearson correlation coefficient between the actual and predicted ages was calculated to assess the prediction accuracy of the model. Finally, permutation tests were implemented to estimate whether the obtained prediction accuracies were significantly higher than a random level (Cole and Franke, 2017; Dosenbach et al., 2010). Specifically, the ages of the training samples were randomly permutated for each prediction model. The p value of the prediction accuracy was obtained by summing the number of permutations that showed a higher correlation coefficient than the actual value of the real model and then divided by the total number of permutations (here we used 1000 times). We applied three feature preprocessing approaches, including the raw features (untreated), scaling and normalization, after which we repeated the whole prediction procedure to evaluate the effects of the preprocessing methods. Finally, we exchanged the training and test samples to perform a cross-validation of the prediction. For the code implementation, the LIBSVM toolbox was used in the SVR model (https://www.csie.ntu.edu.tw/~cjlin/libsvm/) (Chang

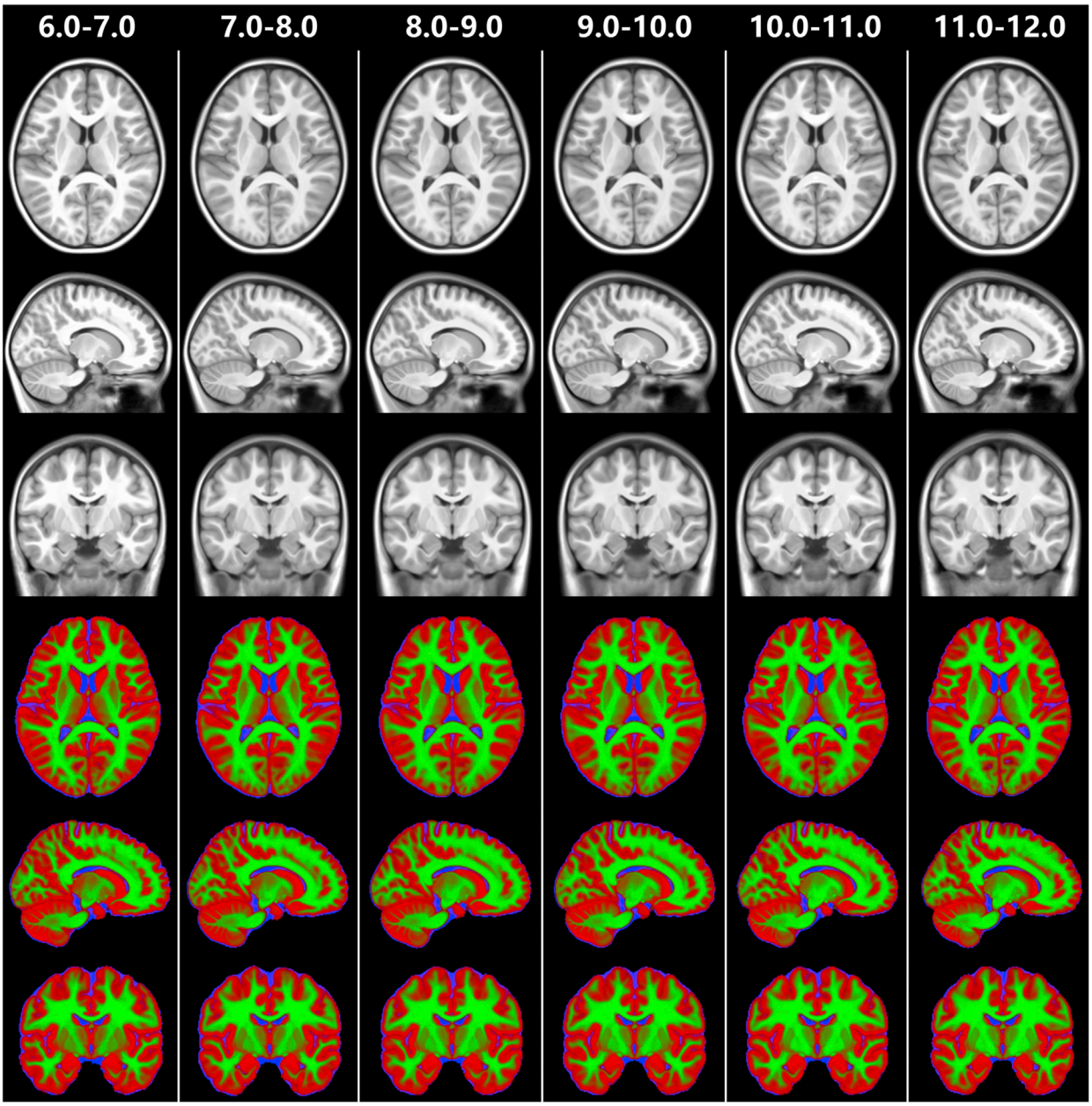

Fig. 5. Detailed slices of the average T1-weighted brain templates (upper panel) and the combined tissue probability atlases (lower panel) of the age subgroups at one-year intervals. Red represents the gray matter, green represents the white matter, and blue represents cerebrospinal fluid. The brain templates are displayed in the neurological convention.

and Lin, 2011), and the PRoNTo toolbox (http://www.mlnl.cs.ucl.ac.uk/pronto/) was used in the RVR model (Schrouff et al., 2013).

We further examined the regional contributions to the prediction model and their differences between the CHN-PD and NIH-PD templates. The voxels with a nonzero regression coefficient/weight in the prediction models trained using both datasets (Datasets 2 and 3) were considered the contributing voxels. The average absolute weight across the voxels in each region in the Brodmann atlas was calculated to represent its importance in the age prediction (Cui and Gong, 2018; Dosenbach et al., 2010; Erus et al., 2014; Siegel et al., 2016). To estimate the regional difference in the contributing weights between the CHN-PD and NIH-PD brain templates, a nonparametric Wilcoxon rank sum test was performed to compare the voxel-wise feature weights of each Brodmann area between these two templates. For each regional test, a Bonferroni-corrected significance level of $p < 0.05$ was adopted for multiple comparisons (here, $p < 0.05/82$, where 82 represents the number of regions in the Brodmann atlas).

2.6. Evaluation of the atlases effects (CHN-PD vs. NIH-PD) on the tissue segmentation accuracy

To further assess the advantages of the proposed CHN-PD atlases in segmenting the brain tissues on Chinese pediatric data, we conducted a comparison (Luo et al., 2014) of the tissue segmentation accuracy between the proposed CHN-PD atlases and the existing NIH-PD atlases using two independent samples (Dataset 2 and Dataset 3). First, we performed an automatic segmentation of the individual T1-weighted images without any prior information (Zhang et al., 2001). These individual-based probabilistic tissue maps of GM, WM and CSF were used as a reference for the subsequent comparison. Then, the segmentation

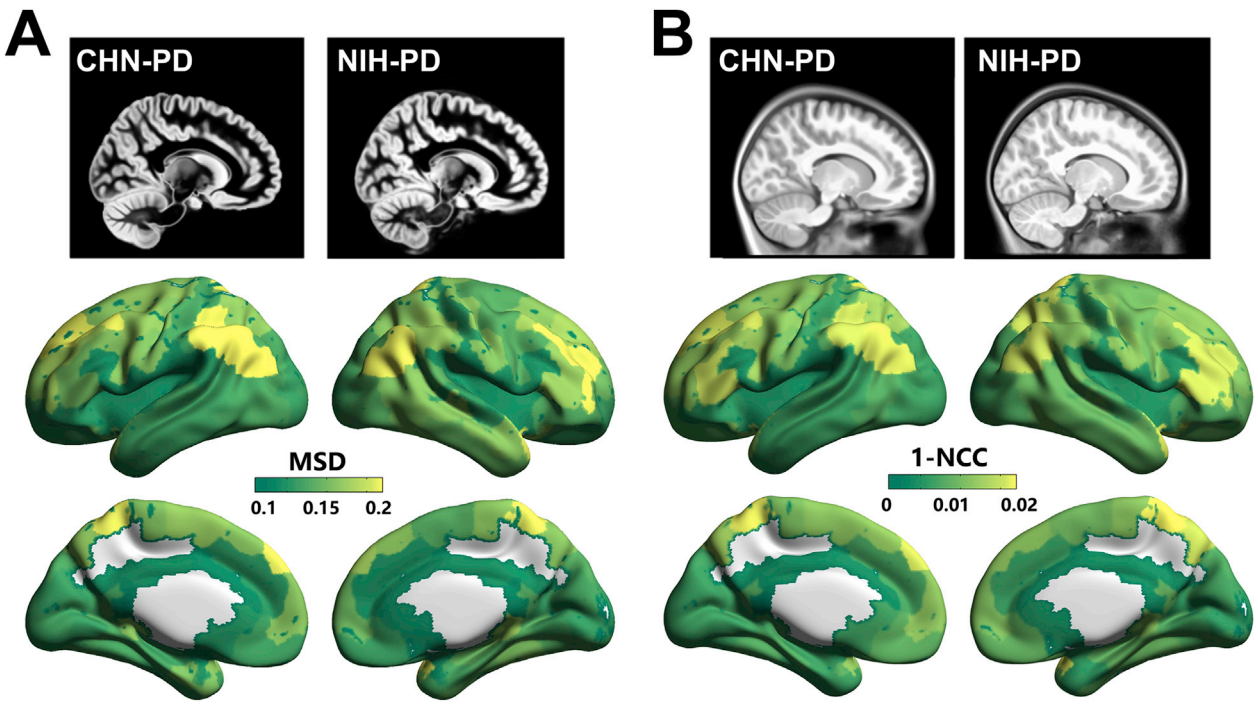

Fig. 6. Regional anatomical differences between the CHN-PD and NIH-PD atlases. Detailed slices of the Chinese pediatric brain atlases and the NIH pediatric brain atlases are shown on the upper panel (A: gray matter probability map; B: T1-weighted brain atlases). Distributions of regional anatomical differences as indicated by the mean square difference (MSD, panel A) and 1 - normalized cross correlation (1 - NCC, panel B) are shown in a 3D surface view with colors from green to yellow representing index values from low to high (lower panel). According to both indexes, the regions with relatively large anatomical differences are located bilaterally in the angular gyri and supramarginal gyri (parts of Wernicke's area), the somatosensory cortices, the dorsolateral prefrontal regions, the inferior frontal gyri (including Broca's area) and the temporopolar cortices. Notably, the CHN-PD atlases were generated using MRI data from Dataset 1 with a group matched to the age (7–11 years) and sex of the group used to generate the NIH-PD atlases. The visualizations of the 3D surface views were generated using BrainNet Viewer software (http://www.nitrc.org/projects/bnv/) (Xia et al., 2013).

was implemented using a prior atlas by separately employing the CHN-PD and NIH-PD brain templates. A range of tissue probability thresholds ($p > 0.1$ to 0.25, at 0.05 intervals) were applied to obtain the final tissue classification. Next, we calculated the Dice coefficient (Dice, 1945) between the individual-based and the Chinese and Caucasian atlas-based tissue classifications. A paired *t*-test was performed on the Dice coefficients to estimate whether the proposed CHN-PD atlas could achieve significant improvements compared with the NIH-PD atlas. A detailed procedure was described in the Supplemental Materials.

2.7. Evaluation of regional anatomical differences between the brain atlases for each age-subgroup and between the sex-specific brain atlases

Similar comparisons were also conducted between the age-specific templates at one-year intervals and between the sex-specific atlases to estimate the regional anatomical differences. Specifically, for the comparisons of age-specific templates, each pair of T1-weighted brain templates in the adjacent age subgroups were initially classified into one group. Then, the Brodmann atlas was nonlinearly warped into the younger age brain template for each group using the ICBM152 nonlinear template as an intermediary to divide the brain into 82 regions. Next, the older brain template and corresponding tissue probabilistic atlas were transformed into the younger template using a nine-parameter affine registration to perform an alignment. For each Brodmann area, the 1-NCC value between each pair of templates was calculated. Similarly, for the comparisons of sex-specific templates, the Brodmann atlas was warped into the female brain template to obtain the regional parcellation, and the male brain template was aligned to the female brain template. Then, the anatomical differences between two templates were assessed for each Brodmann area.

2.8. Comparisons with the diffeomorphic template construction framework

For the CHN-PD brain atlases, we used a well-established ANIMAL registration algorithm (Fonov et al., 2011). One of the most distinctive brain template construction approaches is the diffeomorphic framework (Avants et al., 2011), which guarantees the invertibility and smoothness of the generating transforms during nonlinear registration. We re-created the T1-weighted brain templates for each age subgroup using this framework (implemented in the Advanced Normalization Tools, ANTs pipeline, Avants et al. (2009)) based on the same samples used for the current CHN-PD templates. The hierarchical scheme with 3 iterations at $50 \times 90 \times 20$ registration steps (Avants et al., 2011; Fonov and Collins, 2018) was adopted during the construction process. We used a sharpness index to evaluate whether the use of diffeomorphic registration framework could improve the quality of our proposed templates. A detailed description of the procedure is provided in the Supplemental Materials.

3. Results

3.1. Convergence of the template construction algorithm in the Chinese pediatric atlases

In this study, all types of MRI templates are constructed based on PKU dataset (Dataset 1) through the hierarchical model iteration processes, and qualitative progression is observed along with the iterations. We represent a detailed view of the intermediate models during the construction of the T1 weighted brain template over the full age range (6–12 years old). Fig. 2A illustrates the voxel-wise standard deviation map across the individual scans at different iterations and resolution steps, and Fig. 2B illustrates the corresponding averaged T1-weighted models.

Table 3
Regions showing large anatomical differences between the CHN-PD and NIH-PD atlases.

Brodmann area	MSD	Brodmann area	1-NCC
Left angular gyrus, Wernicke's area (BA 39)	0.244	Right somatosensory association cortex (BA 5)	0.022
Right angular gyrus, Wernicke's area (BA 39)	0.227	Right primary somatosensory cortex (BA 1)	0.019
Right dorsolateral prefrontal cortex (BA 46)	0.224	Left somatosensory cortex (BA 5)	0.018
Left somatosensory cortex (BA 5)	0.224	Right temporopolar (BA 38)	0.017
Left supramarginal gyrus, Wernicke's area (BA 40)	0.223	Left angular gyrus, Wernicke's area (BA 39)	0.017
Left dorsolateral prefrontal cortex (BA 9)	0.221	Left dorsolateral, prefrontal cortex (BA 9)	0.016
Right somatosensory cortex (BA 5)	0.213	Right pars triangularis, Broca's area (BA 45)	0.015
Right temporopolar (BA 38)	0.209	Left supramarginal gyrus, Wernicke's area (BA 40)	0.015
Right primary somatosensory cortex (BA 1)	0.205	Right dorsolateral prefrontal cortex (BA 46)	0.014
Right dorsolateral prefrontal cortex (BA 9)	0.202	Left pars triangularis, Broca's area (BA 45)	0.014
Left dorsolateral prefrontal cortex (BA 46)	0.201	Right visuo-motor coordination (BA 7)	0.014
Right supramarginal gyrus, Wernicke's area (BA 40)	0.200	Right angular gyrus, Wernicke's area (BA 39)	0.014
Right parstriangularis, Broca's area (BA 45)	0.195	Left visuo-motor coordination (BA 7)	0.014
		Left pars opercularis, Broca's area	0.014
		Left temporopolar (BA 38)	0.014

Regions with indexes greater than the mean plus one standard deviation are listed in descending order in the table.

The standard deviation at the voxel level is reduced in each block of four iterations, and the anatomical details gradually become distinct around the neighboring voxels, showing a successful convergence (Fig. 2A and B). The standard T1-weighted *brain* template is generated at the 20th iteration. The root mean square (RMS) of the intensity standard deviation and biases of the average deformation in each iteration step are plotted for all types of MRI templates (Fig. 2C). As the procedure advanced, the RMS progressively decrease across iterations for the averaging models, indicating that the optimization procedure reaches a minimum. Similar convergence processes are found for the averaged *head/brain*, symmetric, and sex-specific templates (Fig. 2C, left panel) and for each age subgroup template (Fig. 2C, right panel).

3.2. Averaged structural MRI atlases for Chinese pediatric brains (CHN-PD atlases)

We generated the T1- (Fig. 3) and T2-weighted (Fig. 4) Chinese pediatric atlases over the full age range (6–12 years). These figures show axial, sagittal and coronal slices of the averaged asymmetric *head/brain* templates, asymmetric sex-specific brain templates and symmetric brain templates. Additionally, Fig. 3 also shows the tissue probability atlases of GM, WM and CSF. In each slice, these templates portray clear anatomical structures in the cerebral and subcortical regions, cerebellum and brainstem. Fig. 5 shows detailed age-specific templates at one-year intervals, including both the T1-weighted brain templates and corresponding tissue probability atlases. A visual inspection indicates similar morphological structures in the brain gyri and sulci across these age-specific templates, and slight anatomical differences in the peripheral GM/WM junctions. All templates are publicly available in the Neuroimaging Informatics Technology Initiative (NIfTI) format in the CHN-PD atlas project on the Neuroimaging Tools and Resources Collaboratory (NITRC) website (https://www.nitrc.org/projects/chn-pd/).

Table 4
Accuracy of the age predictions in different regression frameworks using the CHN-PD and NIH-PD brain atlases as the normalization targets.

Training/Test sample	Dataset 2/Dataset 3		Dataset 3/Dataset 2	
Template	CHN-PD	NIH-PD	CHN-PD	NIH-PD
SVR model				
Raw feature	r = **0.39**	r = 0.36	r = **0.42**	r = 0.35
Scaling	r = **0.40**	r = 0.38	r = **0.44**	r = 0.38
Normalization	r = **0.38**	r = 0.37	r = **0.48**	r = 0.43
RVR model				
Raw feature	r = **0.37**	r = 0.35	r = **0.46**	r = 0.35
Scaling	r = **0.39**	r = 0.38	r = **0.47**	r = 0.37
Normalization	r = **0.38**	r = 0.37	r = **0.48**	r = 0.43

In each comparison between the prediction models adopting the CHN-PD and NIH-PD brain templates, the larger r value is shown in bold. All correlations were significantly greater than a random level ($p < 0.001$, permutation tests).

3.3. Regional anatomical differences between the CHN-PD and NIH-PD atlases

Regarding the absolute differences in the GM probability maps between the CHN-PD and NIH-PD atlases, the regions showing relatively large anatomical differences are located bilaterally in the angular gyri and supramarginal gyri (parts of Wernicke's area), the somatosensory cortices, the dorsolateral prefrontal cortices, the inferior frontal gyri (including Broca's area) and the temporopolar cortices (Fig. 6A, and Table 3). Regarding the spatial similarity across voxels, we show a consistent distribution of anatomical differences in the aforementioned regions between the CHN-PD and NIH-PD atlases (Fig. 6B, and Table 3).

3.4. The CHN-PD atlases display a higher prediction power for the brain age of Chinese pediatric data than the NIH-PD atlases

The results for the predicted brain age are presented in Table 4 and Fig. 7. All correlations are significantly higher than those expected by chance ($p < 0.001$, permutation tests), suggesting that brain age can be successfully predicted by structural features of the individual brain. Notably, the prediction power values are generally higher when using the CHN-PD for image normalization than when using the NIH-PD atlases, regardless of the feature selection and prediction models. The same conclusion is drawn when the training and test samples are exchanged to cross-validate the prediction. According to the statistical analysis, the use of the CHN-PD atlas produces a significantly higher prediction accuracy of brain age than using the NIH-PD atlas across all feature preprocessing operations and regression models ($p = 0.005$, paired *t*-test).

We select the framework showing the highest prediction accuracy, i.e., the SVR model with the normalized feature preprocessing step ($r = 0.48$, Table 4), to show the regional contributions to the predicted age. The regions that are important for predicting age are mainly located in the bilateral entorhinal cortex, perirhinal cortex, somatosensory gyrus and dorsolateral frontal cortex in both the Chinese and NIH pediatric brain templates (Fig. 8A and B). Regarding the differences in the weights of the contributing voxels between the two templates, 30 of 82 regions ($p < 0.05$ after the Bonferroni correction) show significantly different weights for the brain age prediction (Fig. 8C and Table 5). Specifically, compared with the use of the NIH-PD, the use of the CHN-PD reveals significantly greater contributions for the following areas: the bilateral angular gyri (part of Wernicke's area), the right supramarginal gyrus (part of Wernicke's area), the right dorsolateral prefrontal cortex, the left inferior frontal gyrus (including Broca's area) and the somatosensory cortices. In contrast, compared with the use of the CHN-PD, regions

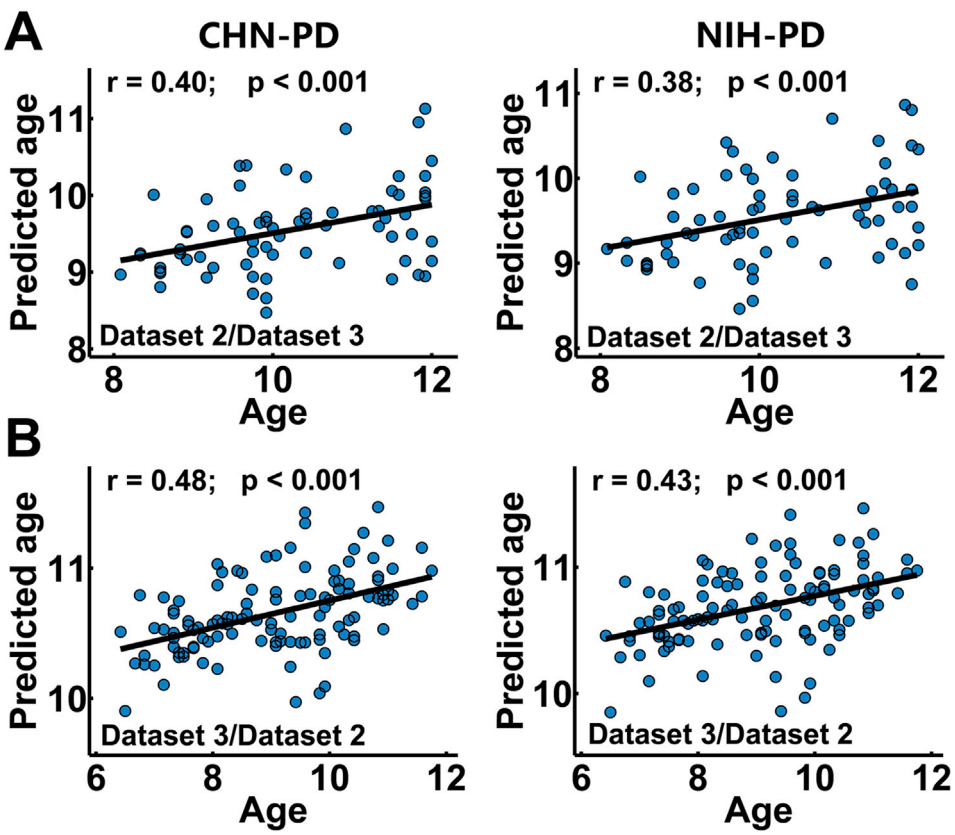

Fig. 7. Effect of the brain atlas choice on the accuracy of the age prediction. Pearson's correlation coefficients between the actual and predicted ages were calculated to represent the prediction accuracy. Using the Chinese children in Datasets 2 and 3 as the training/test samples (marked on the bottom of each figure) in alternation (A and B), the prediction framework employing the Chinese pediatric (CHN-PD) atlases as the normalization target consistently showed a higher accuracy in predicting brain age than the NIH pediatric (NIH-PD) atlases. This plot shows only the SVR model with the scaling feature preprocessing step (A) and the normalization step (B), which obtained the highest prediction accuracy for the corresponding training/test samples. All correlations were significantly greater than the random level ($p < 0.001$, permutation tests). Notably, the CHN-PD atlases were generated using the children in Dataset 1 with a group matched to the age (7–11 years) and sex of the group used to generate the NIH-PD atlases.

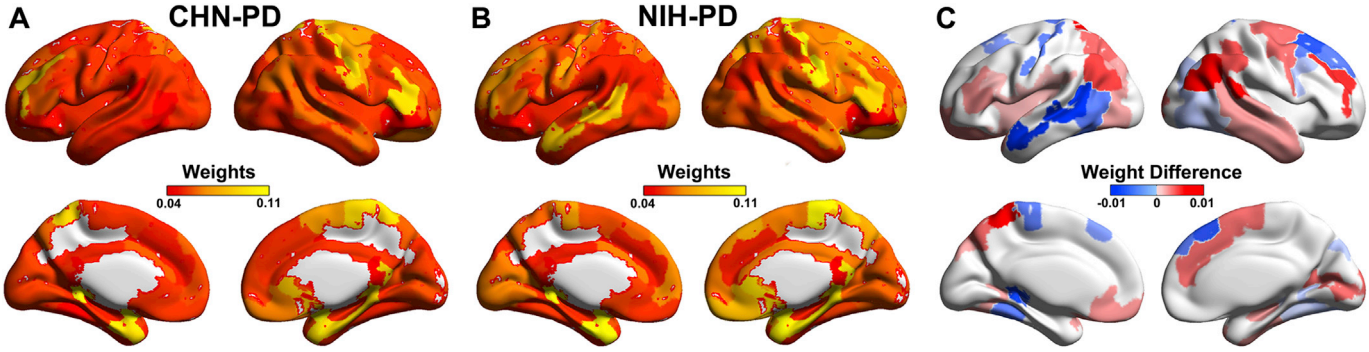

Fig. 8. Regional distribution of the weights of the contributing voxels and their differences between the prediction models applying the CHN-PD and the NIH-PD brain atlases. The average voxel-wise contribution weights of each region in the Brodmann atlas are illustrated separately for the CHN-PD (A) and NIH-PD atlases (B) in color from red to yellow. The regions that showed significant differences in contributing weights in age prediction between the two atlases are shown in 3D surface views (C). Regions colored in red indicate greater contribution weights are obtained using the CHN-PD atlases than the NIH-PD atlases as the normalization target, while regions colored in blue indicate the opposite result. Notably, the CHN-PD atlases were generated using MRI data from Dataset 1 with a group matched to the age (7–11 years) and sex of the group used to generate the NIH-PD atlases. The visualizations of the 3D surface views were generated using the BrainNet Viewer software (http://www.nitrc.org/projects/bnv/) (Xia et al., 2013).

including the lateral temporal cortex, the right dorsolateral frontal cortex and the bilateral frontal eye fields show significantly greater regional contributions in the model employing the NIH-PD atlas.

3.5. The CHN-PD atlases produce a higher tissue segmentation accuracy for Chinese pediatric data than NIH-PD atlases

In both Dataset 2 and Dataset 3, the CHN-PD atlases show a significantly higher accuracy than the NIH-PD atlases in the classification of WM, GM and CSF with probability thresholds ranging from 0.1 to 0.25 (all p-values < 0.001, Fig. 9).

3.6. Comparison with the template sharpness of the diffeomorphic framework

Fig. 10 shows an axial slice of the template for each age-subgroup at one-year intervals using both the ANIMAL registration and ANTs pipeline. As shown in the right panel, the ANIMAL framework exhibits greater sharpness than the diffeomorphic registration at each age interval. Similar results are obtained using the default iteration parameter in ANTs

Table 5
Regional differences in the weights of contributing voxels between the CHN-PD and NIH-PD atlases.

Brodmann area	Difference in weights (CHN-PD > NIH-PD)	p-value
Right angular gyrus, Wernicke's area (BA 39)	0.010	$<10^{-9}$
Left somatosensory association cortex (BA 5)	0.009	$<10^{-9}$
Right premotor cortex and supplementary motor cortex (BA 6)	0.004	$<10^{-9}$
Right dorsolateral prefrontal cortex (BA 46)	0.005	$<10^{-9}$
Left angular gyrus, Wernicke's area (BA 39)	0.005	$<10^{-9}$
Right supramarginal gyrus, Wernicke's area (BA 40)	0.004	$<10^{-9}$
Right inferior temporal gyrus (BA 20)	0.002	$<10^{-9}$
Left associative visual cortex (V3, V4, V5) (BA 19)	0.002	$<10^{-9}$
Right primary auditory cortex (BA 42)	0.007	1.7×10^{-9}
Right primary visual cortex (V1) (BA 17)	0.004	1.7×10^{-8}
Right middle temporal gyrus (BA 21)	0.003	2.9×10^{-7}
Left orbitofrontal area (BA 11)	0.003	3.4×10^{-7}
Left retrosubicular area (BA 48)	0.002	6.8×10^{-7}
Right dorsal anterior cingulate cortex (BA 32)	0.004	2.5×10^{-6}
Left visuo-motor coordination (BA 7)	0.004	3.3×10^{-5}
Left pars triangularis, Broca's area (BA 45)	0.003	4.4×10^{-5}
Left temporopolar (BA 38)	0.002	4.8×10^{-5}
Right primary auditory cortex (BA 41)	0.003	4.9×10^{-5}
Right superior temporal gyrus, Wernicke's area (BA 22)	0.002	5.2×10^{-5}
Brodmann area	**Difference in weights (CHN-PD < NIH-PD)**	**p-value**
Left middle temporal gyrus (BA 21)	−0.010	$<10^{-9}$
Left fusiform gyrus (BA 37)	−0.006	$<10^{-9}$
Right frontal eye fields (BA 8)	−0.008	$<10^{-9}$
Left primary motor cortex (BA 4)	−0.006	$<10^{-9}$
Right dorsolateral prefrontal cortex (BA 9)	−0.006	$<10^{-9}$
Left frontal eye fields (BA 8)	−0.005	$<10^{-9}$
Right associative visual cortex (V3, V4, V5) (BA 19)	−0.003	$<10^{-9}$
Right fusiform gyrus (BA 37)	−0.002	3.5×10^{-9}
Right pars opercularis, Broca's area (BA 44)	−0.003	1.8×10^{-5}
Right primary somatosensory cortex (BA 1)	−0.006	2.8×10^{-5}
Left piriform cortex (BA 27)	−0.009	3.1×10^{-5}

The framework showing the highest prediction accuracy, namely, the SVR model with the normalized feature preprocessing step, was used to show the regional contributions to the age prediction.

(See Fig. S2).

3.7. Regional anatomical differences across age-subgroup and sex-specific atlases

Regarding the age-specific atlases at one-year intervals, the structural differences between each pair of brain templates with adjacent one-year intervals are mainly located in the bilateral dorsolateral and medial frontal and parietal cortices (Fig. 11). The bilateral inferior frontal gyri show relatively large anatomical differences between the early 6- to 7-year old and 7- to 8-year-old brains (Fig. 11). Regarding the sex-specific templates, the regions showing the greatest anatomical difference are mainly located in the right superior frontal gyrus, the bilateral angular gyri and the bilateral supramarginal gyri (parts of Wernicke's area) (Fig. 12).

4. Discussion

In the current study, we constructed a set of Chinese pediatric atlases (CHN-PD) using a large sample of high-quality MR images of Chinese children aged 6–12 years. The CHN-PD atlases include asymmetric and symmetric brain templates, sex-specific brain templates and age-specific brain templates at one-year intervals. The proposed Chinese pediatric atlases showed obvious anatomical differences in the lateral frontal and parietal cortex regions as compared to the NIH-PD atlases. In the Chinese pediatric datasets, both the power of age prediction and the accuracy of tissue segmentation were higher when the CHN-PD atlases were used as the normalization target than when the NIH-PD atlases are employed.

Two previous structural MRI studies have attempted to build Chinese pediatric brain atlases (Luo et al., 2014; Xie et al., 2015). However, several major differences exist between our work and these two earlier studies. First, the pediatric brain atlases proposed here employed high-quality MR images with high signal-to-noise ratios obtained using advanced state-of-the-art 3.0-T Prisma scanners; in contrast, the two previous studies used brain MR images obtained with a 1.5-T MRI scanner (Luo et al., 2014) and a 3.0-T Trio scanner (Xie et al., 2015). Second, our atlases include a larger sample size (N = 328) than the two previous studies (N = 53 and 138, respectively), enabling us to generate pediatric MRI templates at refined one-year intervals. This refinement is important for obtaining an accurate description of the elaborate growth trajectories (e.g., within a one-year period) of children's brains during a phase of rapid and dynamic structural and functional changes (Cao et al., 2016; Giedd et al., 1999; Lebel and Beaulieu, 2011; Levman et al., 2017; Sowell et al., 2003; Walhovd et al., 2017; Zhao et al., 2015). Third, we provide the brain atlases for the whole age range from 6 to 12 years instead of the separate age subgroup templates shown in two previous studies. These atlases are important for future studies designed to predict the "brain age" of Chinese children. Fourth, in contrast to the rigid transformation used in the two previous studies (Luo et al., 2014; Xie et al., 2015), we conducted a nine-parameter affine transformation of the individual images to the initial ICBM152 linear brain target, which reduced the differences in the circumference between the Chinese and Caucasian brains while maintaining compatible regional locations in the Chinese pediatric templates. This approach may benefit future comparative studies investigating the development of brain regions in children from multicultural backgrounds. Fifth, due to the consistent coordinate system of our atlases based on the Montreal Neurological Institute space, the application of our templates is convenient and generalizable. Finally, our brain atlases include symmetric and sex-specific types, which are not included in the two previous studies (Luo et al., 2014; Xie et al., 2015).

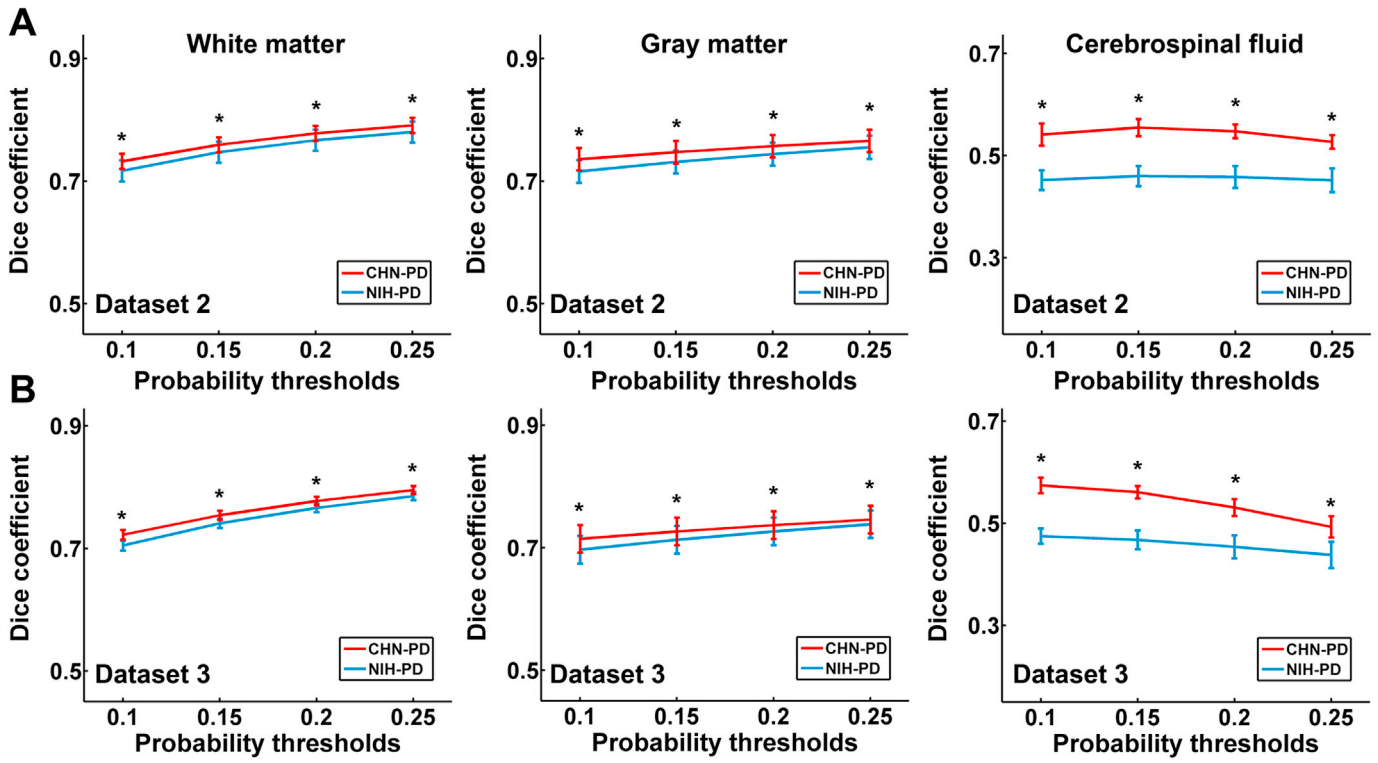

Fig. 9. The tissue segmentation accuracy of the CHN-PD and NIH-PD atlases for Chinese children. The Dice coefficient between each individual-based (using the FAST algorithm without any prior) and two atlas-based segmentations were calculated using two independent datasets. The CHN-PD brain atlases showed a significantly higher overlay with the individual segmentations (as the reference) than the NIH-PD atlases in the classification of WM, GM and CSF with tissue probability thresholds ranging from 0.1 to 0.25 (*, p-value < 0.001). Similar results were obtained from both the HLG dataset (A, Dataset 2) and the healthy ADHD-200 samples (B, Dataset 3). Notably, the CHN-PD atlases were generated using MRI data from Dataset 1 with a group matched to the age (7–11 years) and sex of the group used to generate the NIH-PD template.

Currently, several different strategies have been used to construct brain atlases. We used an unbiased model construction algorithm for the construction of the CHN-PD atlases. This algorithm has been widely used to create MRI templates (De Leener et al., 2018; Fonov et al., 2009, 2011, 2014), which yields abundant anatomical features while maintaining clear tissue contrasts for the templates. Specifically, this iterative construction algorithm captures both the average intensity and the average shape of the brain at a population level. Thus, the use of this approach in combination with our high-quality MRI data from Chinese children is flexible for generating templates for customized age ranges and types. Considering the heterogeneous development of brain regions (Gogtay and Thompson, 2010; Paus, 2005; Toga et al., 2006), our templates with distinct anatomical boundaries and fine details in flexible age ranges may facilitate the description of the accurate spatiotemporal sequence of the brain development of Chinese pediatric population. Another widely used template construction strategy is based on the diffeomorphic framework (Avants et al., 2011). This framework guarantees a smooth and differentiable nonlinear transformation during model iterations. The application of the diffeomorphic framework did not improve the template sharpness in the CHN-PD atlases. These results are consistent with a recent study showing that the use of a strictly diffeomorphic registration does not result in improved sharpness when constructing the adult

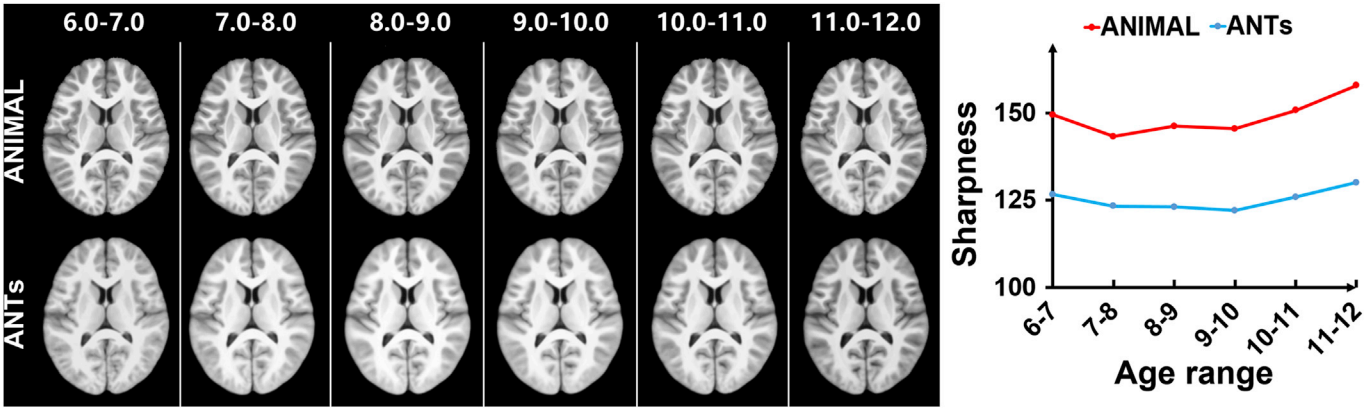

Fig. 10. Differences in the sharpness of the age-subgroup templates between the ANIMAL registration and ANTs pipeline. Left panel: Axial views of templates from each age-subgroup at one-year intervals generated using the ANIMAL registration and ANTs pipeline (diffeomorphic registration). Right panel: The sharpness of templates in each age interval using our ANIMAL (for details, see Methods) and ANTs frameworks. A hierarchical scheme with 3 iterations at $50 \times 90 \times 20$ registration steps was employed during the construction process using the ANTs pipeline (Avants et al., 2011).

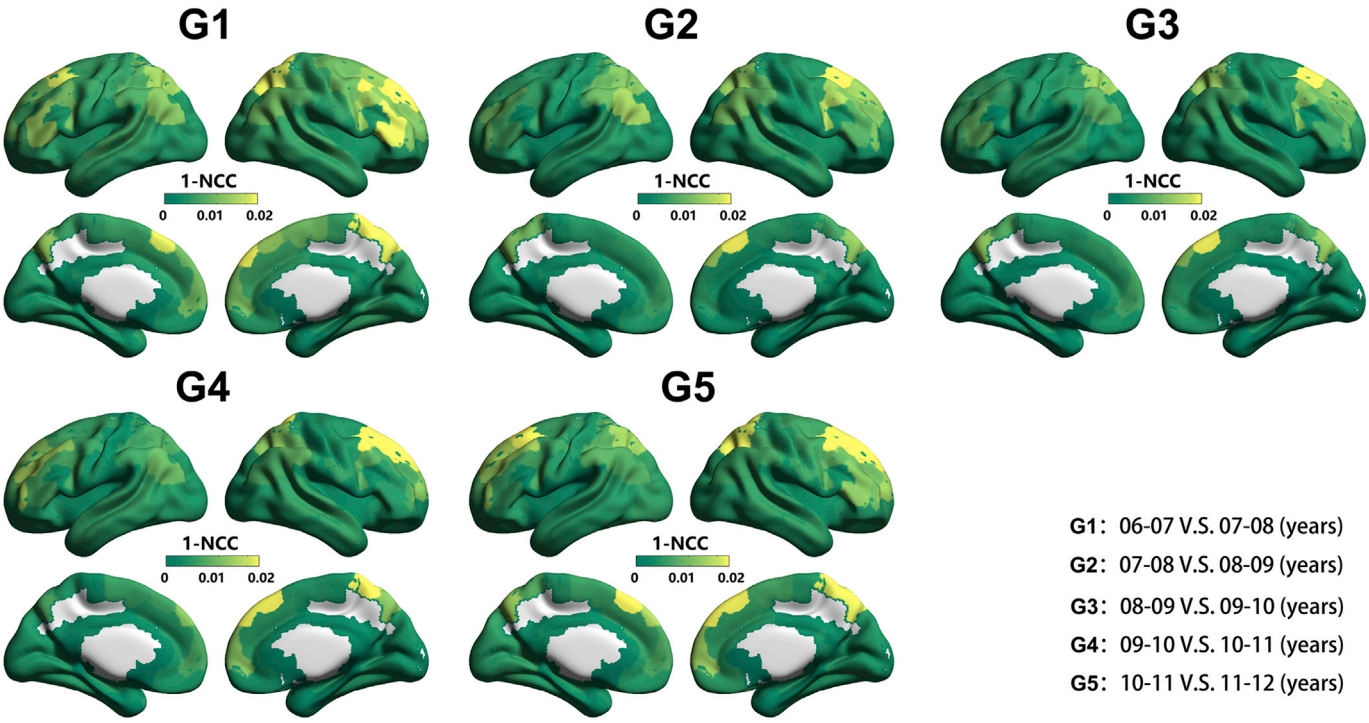

Fig. 11. Regional anatomical differences between two T1-weighted brain templates in each adjacent age subgroup of the CHN-PD atlases. Distributions of regional anatomical differences as indicated by the 1 - normalized cross correlation (NCC) are shown in a 3D surface view with colors ranging from green to yellow representing low to high index values. According to both indexes, the regions with relatively large anatomical differences are mainly located in the bilateral dorsolateral and medial frontal and parietal cortex regions. The bilateral inferior frontal areas showed relatively large anatomical differences between the early 6- to 7-year old group and other age subgroups. The visualizations of the 3D surface views were generated using BrainNet Viewer software (http://www.nitrc.org/projects/bnv/) (Xia et al., 2013).

templates (Fonov and Collins, 2018). Notably, in the present study, the distribution of the samples varied across the different age subgroups, which may affect the consistency of the age-specific templates. However, the number of children per group was not identical because we sought to achieve the maximum utilization of the samples. Although a visual examination did not reveal obvious differences in these age-specific brain atlases (Fig. 5), future studies should consider algorithms, such as adaptive kernel regression (Schuh et al., 2018; Serag et al., 2012), to control for the effect of subject numbers in the different age subgroups.

Several studies have reported significant differences in overall brain morphology (e.g., size, shape and volume) between Chinese and Caucasian brain templates (Tang et al., 2010; Xie et al., 2015). Chinese pediatric brain templates are generally shorter in length and greater in width and height than age-specific American templates (Xie et al., 2015). Our study further extended these structural differences to a detailed regional level (Fig. 6). The regions that showed obvious anatomical differences were mainly located in the bilateral frontal and parietal regions. These regional differences were consistent with the differences reported in previous multicultural studies in which ethnic Chinese adults showed a significantly thinner cortical thickness in the inferior frontal gyrus and supramarginal gyrus (Chee et al., 2011), smaller cortical volume, and larger surface areas in the bilateral superior and medial prefrontal and the bilateral orbitofrontal gyrus (Tang et al., 2018) than Caucasian adults. These consistent results are reasonable since the neuroanatomical development of these areas begins at approximately the time of birth and closely resembles adult levels by the adolescent period (Casey et al., 2005; Thompson and Nelson, 2001). Furthermore, these regions consistently showed different contribution weights in the prediction of brain age between the use of Chinese and Caucasian pediatric brain atlases. The lower prediction accuracy obtained using a mismatched brain template may be driven by the regional differences between the brain templates. Thus, we conclude that the regional structural features captured by the Chinese pediatric atlases may be more representative of the developmental curves of the brains of Chinese children.

Recently, an increasing number of pediatric studies have used the innovative concept of "brain age" to predict the extent of brain maturation (Ball et al., 2017; Brown et al., 2012; Cao et al., 2017; Cole et al., 2017; Dosenbach et al., 2010; Franke et al., 2012; Kwak et al., 2018; Madan and Kensinger, 2018; Zhao et al., 2015, 2019). The predicted age is considered the "brain age" because this value is obtained from a typically developing population and thought to provide a normative maturation curve for pediatric brains with cognitive (Erus et al., 2014) and heritable underlays (Cole and Franke, 2017). Individual deviations from the normal age trajectory of brain development may serve as potential markers of healthy and diseased brains (Cole and Franke, 2017; Dosenbach et al., 2010). An accurate prediction of the brain age is valuable for investigating both typically and atypically developing children. A recent MRI study investigated several methodological factors during image feature generation to improve the accuracy of age prediction (Monté-Rubio et al., 2018). As shown in the present study, the application of Chinese-specific brain templates facilitates the accurate prediction of brain age for the Chinese pediatric population, which is important for future studies.

Several issues need to be further addressed. First, although the sample size used for the template construction was improved, more subjects would certainly be beneficial. Second, we used the cross-subject intensity averaging method to generate the population shape of brain atlases, which is insufficient to preserve the topology of certain brain structures. Previous studies have proposed the use of a Bayesian approach on a diffeomorphic random orbit model to address this issue (Zhang et al., 2014), which needs to be considered further in the future. Third, the proposed CHN-PD atlases were generated using the structural MRI data collected using a 3.0-T MRI scanner. Future studies should determine whether the proposed atlases are appropriate for the children data

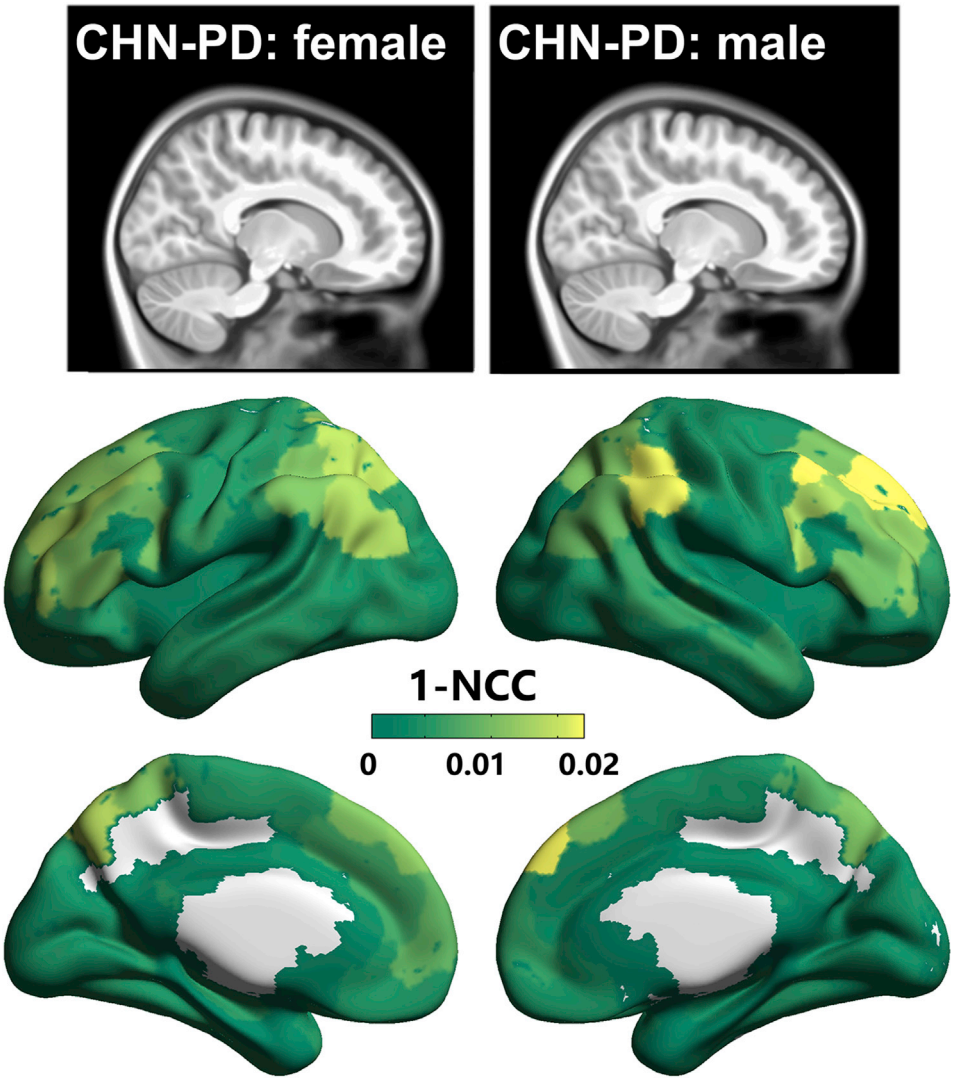

Fig. 12. Regional anatomical differences between the female and male templates of the CHN-PD atlases. Detailed slice of the Chinese female pediatric brain template and the male pediatric brain template are shown on the upper panel. Distributions of regional anatomical differences as indicated by the 1 - normalized cross correlation (NCC) are shown in a 3D surface view with colors ranging from green to yellow representing low to high index values. The regions with relatively large anatomical differences are mainly located in the right superior frontal gyrus and the bilateral angular and supramarginal gyri (parts of Wernicke's area). The visualizations of the 3D surface views were generated using BrainNet Viewer software (http://www.nitrc.org/projects/bnv/) (Xia et al., 2013).

collected using 1.5-T MRI scanners. Fourth, the development of longitudinal or cohort-specific brain atlases using different subpopulations (such as baby brain atlases or disease-related brain atlases) will be important to obtain a comprehensive representation of Chinese children. Fifth, multi-atlas libraries containing templates from other modalities, such as white matter atlases based on diffusion-weighted images, should be established to provide a variety of brain contrasts. Finally, we anticipate that the proposed CHN-PD atlases will be used in future studies investigating the typical and atypical development of Chinese pediatric populations.

Acknowledgments

This work was supported by the National Natural Science Foundation of China (81620108016, 81801783, 31521063 and 31522028, 81571056), Changjiang Scholar Professorship Award (T2015027), Beijing Natural Science Foundation (No. Z161100004916027), Beijing Brain Initiative (Z181100001518003) and the Fundamental Research Funds for the Central Universities (2017XTCX04).

Appendix A. Supplementary data

Supplementary data to this article can be found online at https://doi.org/10.1016/j.neuroimage.2019.01.006.

References

Agcaoglu, O., Miller, R., Mayer, A.R., Hugdahl, K., Calhoun, V.D., 2015. Lateralization of resting state networks and relationship to age and gender. Neuroimage 104, 310–325.
Ashburner, J., Friston, K.J., 1999. Nonlinear spatial normalization using basis functions. Hum. Brain Mapp. 7, 254–266.
Avants, B.B., Duda, J.T., Kilroy, E., Krasileva, K., Jann, K., Kandel, B.T., Tustison, N.J., Yan, L., Jog, M., Smith, R., Wang, Y., Dapretto, M., Wang, D.J., 2015. The pediatric template of brain perfusion. Sci. Data 2, 150003.
Avants, B.B., Tustison, N., Song, G., 2009. Advanced normalization tools (ants). Insight J 2, 1–35.
Avants, B.B., Tustison, N.J., Song, G., Cook, P.A., Klein, A., Gee, J.C., 2011. A reproducible evaluation of ants similarity metric performance in brain image registration. Neuroimage 54, 2033–2044.
Bai, J., Abdul-Rahman, M.F., Rifkin-Graboi, A., Chong, Y.S., Kwek, K., Saw, S.M., Godfrey, K.M., Gluckman, P.D., Fortier, M.V., Meaney, M.J., Qiu, A., 2012. Population differences in brain morphology and microstructure among Chinese, Malay, and indian neonates. PLoS One 7, e47816.
Ball, G., Adamson, C., Beare, R., Seal, M.L., 2017. Modelling neuroanatomical variation during childhood and adolescence with neighbourhood-preserving embedding. Sci. Rep. 7, 17796.
Beaton, A.A., 1997. The relation of planum temporale asymmetry and morphology of the corpus callosum to handedness, gender, and dyslexia: a review of the evidence. Brain Lang. 60, 255–322.
Brown, T.T., Kuperman, J.M., Chung, Y., Erhart, M., McCabe, C., Hagler Jr., D.J., Venkatraman, V.K., Akshoomoff, N., Amaral, D.G., Bloss, C.S., 2012. Neuroanatomical assessment of biological maturity. Curr. Biol. 22, 1693–1698.
Cao, F., Lee, R., Shu, H., Yang, Y., Xu, G., Li, K., Booth, J.R., 2009. Cultural constraints on brain development: evidence from a developmental study of visual word processing in Mandarin Chinese. Cerebr. Cortex 20, 1223–1233.

Cao, M., He, Y., Dai, Z., Liao, X., Jeon, T., Ouyang, M., Chalak, L., Bi, Y., Rollins, N., Dong, Q., 2017. Early development of functional network segregation revealed by connectomic analysis of the preterm human brain. Cerebr. Cortex 27, 1949–1963.
Cao, M., Huang, H., Peng, Y., Dong, Q., He, Y., 2016. Toward developmental connectomics of the human brain. Front. Neuroanat. 10, 25.
Casey, B., Tottenham, N., Liston, C., Durston, S., 2005. Imaging the developing brain: what have we learned about cognitive development? Trends Cognit. Sci. 9, 104–110.
Chang, C.-C., Lin, C.-J., 2011. Libsvm: a library for support vector machines. ACM trans. Intell. Syst. Technol. (TIST) 2, 27.
Chee, M.W.L., Zheng, H., Goh, J.O.S., Park, D., Sutton, B.P., 2011. Brain structure in young and old east asians and westerners: comparisons of structural volume and cortical thickness. J. Cognit. Neurosci. 23, 1065–1079.
Cole, J.H., Franke, K., 2017. Predicting age using neuroimaging: innovative brain ageing biomarkers. Trends Neurosci. 40, 681–690.
Cole, J.H., Poudel, R.P., Tsagkrasoulis, D., Caan, M.W., Steves, C., Spector, T.D., Montana, G., 2017. Predicting brain age with deep learning from raw imaging data results in a reliable and heritable biomarker. Neuroimage 163, 115–124.
Collins, D.L., Holmes, C.J., Peters, T.M., Evans, A.C., 1995. Automatic 3-d model-based neuroanatomical segmentation. Hum. Brain Mapp. 3, 190–208.
Collins, D.L., Zijdenbos, A.P., Kollokian, V., Sled, J.G., Kabani, N.J., Holmes, C.J., Evans, A.C., 1998. Design and construction of a realistic digital brain phantom. IEEE Trans. Med. Imag. 17, 463–468.
Consortium, H.D., 2012. The adhd-200 consortium: a model to advance the translational potential of neuroimaging in clinical neuroscience. Front. Syst. Neurosci. 6, 62.
Cui, Z., Gong, G., 2018. The effect of machine learning regression algorithms and sample size on individualized behavioral prediction with functional connectivity features. Neuroimage 178, 622–637.
Cutter, W.J., Daly, E.M., Robertson, D.M., Chitnis, X.A., van Amelsvoort, T.A., Simmons, A., Ng, V.W., Williams, B.S., Shaw, P., Conway, G.S., 2006. Influence of x chromosome and hormones on human brain development: a magnetic resonance imaging and proton magnetic resonance spectroscopy study of turner syndrome. Biol. Psychiatry 59, 273–283.
Dadar, M., Fonov, V.S., Collins, D.L., Initiative, A.s.D.N., 2018. A comparison of publicly available linear mri stereotaxic registration techniques. Neuroimage 174, 191–200.
De Bellis, M.D., Keshavan, M.S., Beers, S.R., Hall, J., Frustaci, K., Masalehdan, A., Noll, J., Boring, A.M., 2001. Sex differences in brain maturation during childhood and adolescence. Cerebr. Cortex 11, 552–557.
De Leener, B., Fonov, V.S., Collins, D.L., Callot, V., Stikov, N., Cohen-Adad, J., 2018. Pam50: unbiased multimodal template of the brainstem and spinal cord aligned with the icbm152 space. Neuroimage 165, 170–179.
Dickie, D.A., Shenkin, S.D., Anblagan, D., Lee, J., Blesa Cabez, M., Rodriguez, D., Boardman, J.P., Waldman, A., Job, D.E., Wardlaw, J.M., 2017. Whole brain magnetic resonance image atlases: a systematic review of existing atlases and caveats for use in population imaging. Front. Neuroinf. 11, 1.
Dice, L., 1945. Measures of the amount of ecologic association between species. Ecology 26, 297–302.
Dong, Q., Lin, C., 2011. Standardized Tests of the National Children's Study of china. Science Press, Beijing.
Dosenbach, N.U., Nardos, B., Cohen, A.L., Fair, D.A., Power, J.D., Church, J.A., Nelson, S.M., Wig, G.S., Vogel, A.C., Lessov-Schlaggar, C.N., Barnes, K.A., Dubis, J.W., Feczko, E., Coalson, R.S., Pruett Jr., J.R., Barch, D.M., Petersen, S.E., Schlaggar, B.L., 2010. Prediction of individual brain maturity using fmri. Science 329, 1358–1361.
Drucker, H., Burges, C.J., Kaufman, L., Smola, A.J., Vapnik, V., 1997. Support vector regression machines. Adv. Neural Inf. Process. Syst. 155–161.
Erus, G., Battapady, H., Satterthwaite, T.D., Hakonarson, H., Gur, R.E., Davatzikos, C., Gur, R.C., 2014. Imaging patterns of brain development and their relationship to cognition. Cerebr. Cortex 25, 1676–1684.
Evans, A.C., Janke, A.L., Collins, D.L., Baillet, S., 2012. Brain templates and atlases. Neuroimage 62, 911–922.
Evans, T.M., Flowers, D.L., Napoliello, E.M., Eden, G.F., 2014. Sex-specific gray matter volume differences in females with developmental dyslexia. Brain Struct. Funct. 219, 1041–1054.
Fair, D.A., Nigg, J.T., Iyer, S., Bathula, D., Mills, K.L., Dosenbach, N.U., Schlaggar, B.L., Mennes, M., Gutman, D., Bangaru, S., Buitelaar, J.K., Dickstein, D.P., Di Martino, A., Kennedy, D.N., Kelly, C., Luna, B., Schweitzer, J.B., Velanova, K., Wang, Y.F., Mostofsky, S., Castellanos, F.X., Milham, M.P., 2012. Distinct neural signatures detected for adhd subtypes after controlling for micro-movements in resting state functional connectivity mri data. Front. Syst. Neurosci. 6, 80.
Fonov, V., Collins, D.L., 2018. Comparison of Different Methods for Average Anatomical Templates Creation: Do We Really Gain Anything from a Diffeomorphic Framework? bioRxiv, p. 277087.
Fonov, V., Evans, A.C., Botteron, K., Almli, C.R., McKinstry, R.C., Collins, D.L., Brain Development Cooperative, G., 2011. Unbiased average age-appropriate atlases for pediatric studies. Neuroimage 54, 313–327.
Fonov, V.S., Evans, A.C., McKinstry, R.C., Almli, C., Collins, D., 2009. Unbiased nonlinear average age-appropriate brain templates from birth to adulthood. Neuroimage S102.
Fonov, V.S., Le Troter, A., Taso, M., De Leener, B., Lévêque, G., Benhamou, M., Sdika, M., Benali, H., Pradat, P.-F., Collins, D.L., 2014. Framework for integrated mri average of the spinal cord white and gray matter: the mni–poly–amu template. Neuroimage 102, 817–827.
Franke, K., Luders, E., May, A., Wilke, M., Gaser, C., 2012. Brain maturation: predicting individual brainage in children and adolescents using structural mri. Neuroimage 63, 1305–1312.
Gennatas, E.D., Avants, B.B., Wolf, D.H., Satterthwaite, T.D., Ruparel, K., Ciric, R., Hakonarson, H., Gur, R.E., Gur, R.C., 2017. Age-related effects and sex differences in gray matter density, volume, mass, and cortical thickness from childhood to young adulthood. J. Neurosci. 3550-3516.
Giedd, J.N., Blumenthal, J., Jeffries, N.O., Castellanos, F.X., Liu, H., Zijdenbos, A., Paus, T., Evans, A.C., Rapoport, J.L., 1999. Brain development during childhood and adolescence: a longitudinal mri study. Nat. Neurosci. 2, 861–863.
Gogtay, N., Thompson, P.M., 2010. Mapping gray matter development: implications for typical development and vulnerability to psychopathology. Brain Cogn. 72, 6–15.
Good, C.D., Johnsrude, I., Ashburner, J., Henson, R.N., Friston, K.J., Frackowiak, R.S., 2001. Cerebral asymmetry and the effects of sex and handedness on brain structure: a voxel-based morphometric analysis of 465 normal adult human brains. Neuroimage 14, 685–700.
Guimond, A., Meunier, J., Thirion, J.-P., 1998. Automatic computation of average brain models. In: International Conference on Medical Image Computing and Computer-Assisted Intervention. Springer, pp. 631–640.
Guimond, A., Roche, A., Ayache, N., Meunier, J., 2001. Multimodal brain warping using the demons algorithm and adaptative intensity corrections. IEEE Trans. Med. Imag. 20, 58–69.
Guo, X., Chen, C., Chen, K., Jin, Z., Peng, D., Yao, L., 2007. Brain development in Chinese children and adolescents: a structural mri study. Neuroreport 18, 875–880.
Herbert, M.R., Harris, G.J., Adrien, K.T., Ziegler, D.A., Makris, N., Kennedy, D.N., Lange, N.T., Chabris, C.F., Bakardjiev, A., Hodgson, J., 2002. Abnormal asymmetry in language association cortex in autism. Ann. Neurol.: Official J. Am. Neurol. Assoc. Child Neurol. Soc. 52, 588–596.
Holden, M., Hill, D.L., Denton, E.R., Jarosz, J.M., Cox, T.C., Rohlfing, T., Goodey, J., Hawkes, D.J., 2000. Voxel similarity measures for 3-d serial mr brain image registration. IEEE Trans. Med. Imag. 19, 94–102.
Kwak, S., Kim, H., Chey, J., Youm, Y., 2018. Feeling how old i am: subjective age is associated with estimated brain age. Front. Aging Neurosci. 10, 168.
Lancaster, J.L., Tordesillas-Gutierrez, D., Martinez, M., Salinas, F., Evans, A., Zilles, K., Mazziotta, J.C., Fox, P.T., 2007. Bias between mni and talairach coordinates analyzed using the icbm-152 brain template. Hum. Brain Mapp. 28, 1194–1205.
Lebel, C., Beaulieu, C., 2011. Longitudinal development of human brain wiring continues from childhood into adulthood. J. Neurosci. 31, 10937–10947.
Leonard, C.M., Eckert, M.A., 2008. Asymmetry and dyslexia. Dev. Neuropsychol. 33, 663–681.
Levman, J., MacDonald, P., Lim, A.R., Forgeron, C., Takahashi, E., 2017. A pediatric structural mri analysis of healthy brain development from newborns to young adults. Hum. Brain Mapp.
Liang, P., Shi, L., Chen, N., Luo, Y., Wang, X., Liu, K., Mok, V.C.T., Chu, W.C.W., Wang, D., Li, K., 2015. Construction of brain atlases based on a multi-center mri dataset of 2020 Chinese adults. Sci. Rep. 5.
Luo, Y., Shi, L., Weng, J., He, H., Chu, W.C., Chen, F., Wang, D., 2014. Intensity and sulci landmark combined brain atlas construction for Chinese pediatric population. Hum. Brain Mapp. 35, 3880–3892.
Madan, C.R., Kensinger, E.A., 2018. Predicting age from cortical structure across the lifespan. Eur. J. Neurosci. 47, 399–416.
Marcus, D.S., Harms, M.P., Snyder, A.Z., Jenkinson, M., Wilson, J.A., Glasser, M.F., Barch, D.M., Archie, K.A., Burgess, G.C., Ramaratnam, M., 2013. Human connectome project informatics: quality control, database services, and data visualization. Neuroimage 80, 202–219.
Mei, L., Xue, G., Lu, Z.-L., Chen, C., Wei, M., He, Q., Dong, Q., 2015. Long-term experience with Chinese language shapes the fusiform asymmetry of English reading. Neuroimage 110, 3–10.
Monté-Rubio, G.C., Falcón, C., Pomarol-Clotet, E., Ashburner, J., 2018. A comparison of various mri feature types for characterizing whole brain anatomical differences using linear pattern recognition methods. Neuroimage.
Murphy, D.G., DeCarli, C., Daly, E., Haxby, J.V., Allen, G., McIntosh, A., Horwitz, B., Rapoport, S., Schapiro, M., White, B., 1993. X-chromosome effects on female brain: a magnetic resonance imaging study of turner's syndrome. Lancet 342, 1197–1200.
Nyúl, L.G., Udupa, J.K., 1999. On standardizing the mr image intensity scale. Magn. Reson. Med.: Official J. Int. Soc. Magn. Res. Med. 42, 1072–1081.
Oishi, K., Chang, L., Huang, H., 2019. Baby brain atlases. Neuroimage 185, 865–880.
Paus, T., 2005. Mapping brain maturation and cognitive development during adolescence. Trends Cognit. Sci. 9, 60–68.
Peper, J.S., van den Heuvel, M.P., Mandl, R.C., Pol, H.E.H., van Honk, J., 2011. Sex steroids and connectivity in the human brain: a review of neuroimaging studies. Psychoneuroendocrinology 36, 1101–1113.
Richards, J.E., Sanchez, C., Phillips-Meek, M., Xie, W., 2016. A database of age-appropriate average mri templates. Neuroimage 124, 1254–1259.
Richards, J.E., Xie, W., 2015. Brains for all the ages: structural neurodevelopment in infants and children from a life-span perspective. Adv. Child Dev. Behav. 1–52. Elsevier.
Sanchez, C.E., Richards, J.E., Almli, C.R., 2012. Age-specific mri templates for pediatric neuroimaging. Dev. Neuropsychol. 37, 379–399.
Schrouff, J., Rosa, M.J., Rondina, J.M., Marquand, A.F., Chu, C., Ashburner, J., Phillips, C., Richiardi, J., Mourão-Miranda, J., 2013. Pronto: pattern recognition for neuroimaging toolbox. Neuroinformatics 11, 319–337.
Schuh, A., Makropoulos, A., Robinson, E.C., Cordero-Grande, L., Hughes, E., Hutter, J., Price, A., Murgasova, M., Teixeira, R.P.A., Tusor, N., 2018. Unbiased Construction of a Temporally Consistent Morphological Atlas of Neonatal Brain Development. bioRxiv, p. 251512.
Serag, A., Aljabar, P., Ball, G., Counsell, S.J., Boardman, J.P., Rutherford, M.A., Edwards, A.D., Hajnal, J.V., Rueckert, D., 2012. Construction of a consistent high-definition spatio-temporal atlas of the developing brain using adaptive kernel regression. Neuroimage 59, 2255–2265.

Shaw, P., Lalonde, F., Lepage, C., Rabin, C., Eckstrand, K., Sharp, W., Greenstein, D., Evans, A., Giedd, J., Rapoport, J., 2009. Development of cortical asymmetry in typically developing children and its disruption in attention-deficit/hyperactivity disorder. Arch. Gen. Psychiatr. 66, 888–896.
Siegel, J.S., Ramsey, L.E., Snyder, A.Z., Metcalf, N.V., Chacko, R.V., Weinberger, K., Baldassarre, A., Hacker, C.D., Shulman, G.L., Corbetta, M., 2016. Disruptions of network connectivity predict impairment in multiple behavioral domains after stroke. Proc. Natl. Acad. Sci. Unit. States Am. 113, E4367–E4376.
Siok, W.T., Niu, Z., Jin, Z., Perfetti, C.A., Tan, L.H., 2008. A structural–functional basis for dyslexia in the cortex of Chinese readers. Proc. Natl. Acad. Sci. Unit. States Am. 105, 5561–5566.
Siok, W.T., Perfetti, C.A., Jin, Z., Tan, L.H., 2004. Biological abnormality of impaired reading is constrained by culture. Nature 431, 71.
Smith, S.M., 2002. Fast robust automated brain extraction. Hum. Brain Mapp. 17, 143–155.
Smith, S.M., Jenkinson, M., Woolrich, M.W., Beckmann, C.F., Behrens, T.E., Johansen-Berg, H., Bannister, P.R., De Luca, M., Drobnjak, I., Flitney, D.E., Niazy, R.K., Saunders, J., Vickers, J., Zhang, Y., De Stefano, N., Brady, J.M., Matthews, P.M., 2004. Advances in functional and structural mr image analysis and implementation as fsl. Neuroimage 23 (Suppl. 1). S208-219.
Song, J.W., Mitchell, P.D., Kolasinski, J., Ellen Grant, P., Galaburda, A.M., Takahashi, E., 2014. Asymmetry of white matter pathways in developing human brains. Cerebr. Cortex 25, 2883–2893.
Sowell, E.R., Peterson, B.S., Thompson, P.M., Welcome, S.E., Henkenius, A.L., Toga, A.W., 2003. Mapping cortical change across the human life span. Nat. Neurosci. 6, 309–315.
Tang, Y., Hojatkashani, C., Dinov, I.D., Sun, B., Fan, L., Lin, X., Qi, H., Hua, X., Liu, S., Toga, A.W., 2010. The construction of a Chinese mri brain atlas: a morphometric comparison study between Chinese and caucasian cohorts. Neuroimage 51, 33–41.
Tang, Y., Zhao, L., Lou, Y., Shi, Y., Fang, R., Lin, X., Liu, S., Toga, A., 2018. Brain structure differences between Chinese and caucasian cohorts: a comprehensive morphometry study. Hum. Brain Mapp. 39, 2147–2155.
Thompson, R.A., Nelson, C.A., 2001. Developmental science and the media: early brain development. Am. Psychol. 56, 5.
Tipping, M.E., 2001. Sparse bayesian learning and the relevance vector machine. J. Mach. Learn. Res. 1, 211–244.
Toga, A.W., Thompson, P.M., 2003. Mapping brain asymmetry. Nat. Rev. Neurosci. 4, 37.
Toga, A.W., Thompson, P.M., Sowell, E.R., 2006. Mapping brain maturation. Trends Neurosci. 29, 148–159.
Tustison, N.J., Avants, B.B., Cook, P.A., Zheng, Y., Egan, A., Yushkevich, P.A., Gee, J.C., 2010. N4itk: improved n3 bias correction. IEEE Trans. Med. Imag. 29, 1310–1320.
Uchiyama, H.T., Seki, A., Tanaka, D., Koeda, T., Jcs, G., 2013. A study of the standard brain in Japanese children: morphological comparison with the mni template. Brain Dev. 35, 228–235.
Vértes, P.E., Bullmore, E.T., 2015. Annual research review: growth connectomics–the organization and reorganization of brain networks during normal and abnormal development. JCPP (J. Child Psychol. Psychiatry) 56, 299–320.
Walhovd, K.B., Fjell, A.M., Giedd, J., Dale, A.M., Brown, T.T., 2017. Through thick and thin: a need to reconcile contradictory results on trajectories in human cortical development. Cerebr. Cortex 27, 1472–1481.
Wilke, M., Holland, S.K., Altaye, M., Gaser, C., 2008. Template-o-matic: a toolbox for creating customized pediatric templates. Neuroimage 41, 903–913.
Wilke, M., Schmithorst, V.J., Holland, S.K., 2002. Assessment of spatial normalization of whole-brain magnetic resonance images in children. Hum. Brain Mapp. 17, 48–60.
Wu, D., Ma, T., Ceritoglu, C., Li, Y., Chotiyanonta, J., Hou, Z., Hsu, J., Xu, X., Brown, T., Miller, M.I., 2016. Resource atlases for multi-atlas brain segmentations with multiple ontology levels based on t1-weighted mri. Neuroimage 125, 120–130.
Xia, M., Wang, J., He, Y., 2013. Brainnet viewer: a network visualization tool for human brain connectomics. PLoS One 8, e68910.
Xie, W., Richards, J.E., Lei, D., Lee, K., Gong, Q., 2014. Comparison of the brain development trajectory between Chinese and u.S. Children and adolescents. Front. Syst. Neurosci. 8, 249.
Xie, W., Richards, J.E., Lei, D., Zhu, H., Lee, K., Gong, Q., 2015. The construction of mri brain/head templates for Chinese children from 7 to 16 years of age. Dev. Cogn. Neurosci. 15, 94–105.
Xue, G., Dong, Q., Chen, K., Jin, Z., Chen, C., Zeng, Y., Reiman, E.M., 2005. Cerebral asymmetry in children when reading Chinese characters. Cognit. Brain Res. 24, 206–214.
Yoon, U., Fonov, V.S., Perusse, D., Evans, A.C., Brain Development Cooperative, G., 2009. The effect of template choice on morphometric analysis of pediatric brain data. Neuroimage 45, 769–777.
Zhang, Y., Brady, M., Smith, S., 2001. Segmentation of brain mr images through a hidden markov random field model and the expectation-maximization algorithm. IEEE Trans. Med. Imag. 20, 45–57.
Zhang, Y., Zhang, J., Hsu, J., Oishi, K., Faria, A.V., Albert, M., Miller, M.I., Mori, S., 2014. Evaluation of group-specific, whole-brain atlas generation using volume-based template estimation (vte): application to normal and alzheimer's populations. Neuroimage 84, 406–419.
Zhao, F., Huang, Q., Gao, W., 2006. Image matching by normalized cross-correlation. Acoustics, speech and signal processing. In: 2006. ICASSP 2006 Proceedings. 2006 IEEE International Conference on. IEEE. II-II).
Zhao, T., Cao, M., Niu, H., Zuo, X.-N., Evans, A., He, Y., Dong, Q., Shu, N., 2015. Age-related changes in the topological organization of the white matter structural connectome across the human lifespan. Hum. Brain Mapp. 36, 3777–3792.
Zhao, T., Mishra, V., Jeon, T., Ouyang, M., Peng, Q., Chalak, L., Wisnowski, J.L., Heyne, R., Rollins, N., Shu, N., Huang, H., 2019. Structural network maturation of the preterm human brain. Neuroimage 185, 699–710.
Zhong, S., He, Y., Shu, H., Gong, G., 2016. Developmental changes in topological asymmetry between hemispheric brain white matter networks from adolescence to young adulthood. Cerebr. Cortex 27, 2560–2570.
Zhou, D., Lebel, C., Evans, A., Beaulieu, C., 2013. Cortical thickness asymmetry from childhood to older adulthood. Neuroimage 83, 66–74.